

Copyright  
by  
Han-Jong Chia  
2009

The Dissertation Committee for Han-Jong Chia  
certifies that this is the approved version of the following dissertation:

**Force Detected Nuclear Magnetic Resonance on  
(NH<sub>4</sub>)<sub>2</sub>SO<sub>4</sub> and MgB<sub>2</sub>**

Committee:

---

John T. Markert, Supervisor

---

Alex de Lozanne

---

Chih-Kang Shih

---

Zhen Yao

---

Li Shi

**Force Detected Nuclear Magnetic Resonance on  
(NH<sub>4</sub>)<sub>2</sub>SO<sub>4</sub> and MgB<sub>2</sub>**

by

**Han-Jong Chia, B.A.**

**DISSERTATION**

Presented to the Faculty of the Graduate School of  
The University of Texas at Austin  
in Partial Fulfillment  
of the Requirements  
for the Degree of

**DOCTOR OF PHILOSOPHY**

THE UNIVERSITY OF TEXAS AT AUSTIN

December 2009

Dedicated to my family.

## Acknowledgments

John Markert has been invaluable to my development as a graduate student. He has given me a great deal of freedom to pursue my research goals but always provides sound advice when I appear to be heading in the wrong direction or asks me questions that make me reevaluate how well I understand a concept. Yong Lee was nice enough to take me under his wing and teach me everything he knows about NMRFM. Without observing how he thinks and his work ethic I wouldn't be where I am today. Wei Lu and Utkur Mirsaidov helped me greatly to understand many lab concepts when I first joined the lab. Keeseong Park was a great office companion especially during the long nights in the lab.

Mark Monti helped enormously in getting the He-3 probe to work because he was able to come up with imaginative alternative methods to techniques we had assumed to be sound. Without his help half of this dissertation would be empty. Isaac Manzanera Esteve and Rosa Cardenas always asked me intriguing questions that helped me better understand many concepts I thought I was an expert on. They also provided the lab with a cheerful atmosphere that was always welcome. Jeremy Paster helped me look through some data and I wish him luck in taking over the He-3 probe.

Alex de Lozanne and his students have helped me greatly through my

graduate career. I'd like to thank Changbae Hyun and Junwei Huang for the advice they provided me. Tien-Ming Chuang and Jeehoon Kim through their postdoc experiences gave me great advice on how to improve my probe. Alfred Lee has also been helpful with his MFM knowledge.

Ken Shih for accepting me into IGERT and giving me the chance to broaden my outlook on materials physics and nanoscience. The connections I've made through IGERT have helped me greatly refine my research outlook. Insun Jo for letting me borrow some things from his lab.

Lanny Sandefur and Ed Baez helpfully filled thousands of liters of liquid helium and nitrogen for me. Their help in leak checking my probe was also instrumental for getting our low temperature experiments off the ground. Jack Clifford and Allen Schroeder and his staff are one of the best machine shops in the country and they helped greatly to get the precise components I needed.

My collaborators Costel Constantin and Jae-Hyuk Choi have given me the chance to learn about new subjects and help to contribute to their interesting projects.

My numerous friends that I play baseball and tennis with always gave me something to look forward to when things weren't going well in the lab. They've helped me meet more friends than I can count and have been a major part of my life outside of school.

Lastly I'd like to thank my wife Yi-Hui Wu. She and our cat Jasper Lao-Mao Wu-Chia have made my graduate school experience infinitely more

enjoyable that I could have ever thought possible.

# Force Detected Nuclear Magnetic Resonance on $(\text{NH}_4)_2\text{SO}_4$ and $\text{MgB}_2$

Publication No. \_\_\_\_\_

Han-Jong Chia, Ph.D.

The University of Texas at Austin, 2009

Supervisor: John T. Markert

Nuclear magnetic resonance force microscopy (NMRFM) is a technique that combines aspects of scanning probe microscopy (SPM) and nuclear magnetic resonance (NMR) to obtain 3 dimensional nanoscale spatial resolution and perform spectroscopy. We describe the components of a helium-3 NMRFM probe and studies of ammonium sulfate ( $(\text{NH}_4)_2\text{SO}_4$ ) and magnesium dibordie ( $\text{MgB}_2$ ). For our room temperature  $(\text{NH}_4)_2\text{SO}_4$  studies we were able to perform a 1-D scan and perform nutation and spin echo experiments. In our 77 K  $\text{MgB}_2$  we demonstrate a 1-D scan of a 30  $\mu\text{m}$  powder sample. In addition, we describe magnetic measurements of the possible dilute semiconductors  $\text{Mn}_x\text{Sc}_{1-x}\text{N}$  and  $\text{Fe}_{0.1}\text{Sc}_{0.9}\text{N}$ .



# Table of Contents

<b>Acknowledgments</b>	<b>v</b>
<b>Abstract</b>	<b>viii</b>
<b>List of Figures</b>	<b>xi</b>
<b>Chapter 1. Introduction to Nuclear Magnetic Resonance and Magnetic Resonance Force Microscopy</b>	<b>1</b>
1.1 Basics of magnetic resonance and polarization . . . . .	1
1.2 Spins in the lab and rotating frame . . . . .	5
1.3 Spin relaxation . . . . .	8
1.4 Experimental setup for conventional NMR . . . . .	12
1.5 Magnetic Resonance Force Microscopy . . . . .	13
1.6 Sensitivity of MRFM vs. conventional NMR . . . . .	16
1.7 Cyclic adiabatic inversion . . . . .	19
1.8 Resonance slice and imaging . . . . .	22
<b>Chapter 2. Experimental details of magnetic resonance force microscopy</b>	<b>24</b>
2.1 He-3 cryostat . . . . .	24
2.2 Probehead . . . . .	25
2.3 Attocube-type positioners . . . . .	28
2.4 Capacitor position sensor . . . . .	32
2.5 Cantilevers . . . . .	35
2.6 Fiber interferometer . . . . .	40
2.7 RF circuitry . . . . .	42
2.8 Lock-in detection . . . . .	47
2.9 Variable temperature insert . . . . .	50
2.10 RF artifact . . . . .	50

2.11 Gradient magnet . . . . .	51
2.12 Achieving resonance . . . . .	55
<b>Chapter 3. Initial room temperature experiment on ammonium sulfate</b>	<b>58</b>
3.1 Conventional NMR . . . . .	58
3.2 Experimental Details of Room Temperature Scan . . . . .	60
<b>Chapter 4. NMRFM studies of Magnesium Diboride</b>	<b>74</b>
4.1 Magnesium diboride background . . . . .	74
4.2 NMRFM experimental considerations . . . . .	78
4.3 Preliminary NMRFM data on $\text{MgB}_2$ . . . . .	80
<b>Chapter 5. Magnetic Measurements of <math>\text{Mn}_x\text{Sc}_{1-x}\text{N}</math> and <math>\text{Fe}_{0.1}\text{Sc}_{0.9}\text{N}</math>, possible dilute magnetic semiconductors</b>	<b>85</b>
5.1 Background . . . . .	85
5.2 MBE growth of films . . . . .	89
5.3 SQUID data . . . . .	89
<b>Bibliography</b>	<b>98</b>
<b>Appendices</b>	<b>103</b>
<b>Appendix</b>	<b>104</b>
<b>Vita</b>	<b>105</b>

## List of Figures

1.1	Zeeman level splitting for $I = 1/2$ . . . . .	3
1.2	Magnetic moment $\vec{\mu}$ precessing about $\vec{H}_0$ . . . . .	6
1.3	$\vec{\mu}$ rotating about $H_{eff}$ once $\vec{H}_1$ is applied . . . . .	8
1.4	a) A $\pi/2$ pulse rotates the spins $90^\circ$ ; b) the spins decohere in the transverse plane producing a FID; c) the spins are flipped $180^\circ$ by a $\pi$ pulse; and d) the spins reform their coherence resulting in a spin echo. . . . .	10
1.5	Setup for conventional coil NMR. . . . .	12
1.6	Setup for sample-on-oscillator MRFM . . . . .	15
1.7	a) cyclic adiabatic inversion with amplitude $\Omega$ and frequency $1/\omega_{osc}$ about the resonance field $\omega$ . b) In the lab frame the spins move above and below the transverse plane with amplitude $\Omega$ . . . . .	20
1.8	$\pi/2$ - $\tau$ - $\pi$ - $t$ - $\pi/2$ - $\tau_x$ -CAI where $\tau_x$ is varied to obtain the spin echo. The spin echo is shown above where the center occurs at $2\tau$ . From this plot we can see that by choosing $t$ smaller than $\tau$ we have obtained a point on the spin echo far from its peak. . . . .	21
1.9	a) Resonance slice shape for a magnet with shape. b). Notice that the thickness of the slice is not constant and depends on the position. Equation 1.37 applies only for one particular point in space that has a particular field gradient [23]. . . . .	23
2.1	Microscope head of the He-3 probe . . . . .	26
2.2	Blow up of the microscope head . . . . .	27
2.3	3-D CAD drawing of Attocube stages [18] . . . . .	29
2.4	a) Initial state of the stage, b) The piezo is slowly expanded by a rising voltage causing the clamp and graphite rod to move forward as well. c) The voltage applied to the piezo is rapidly ramped to zero causing the piezo to retract. The graphite rod “slips” within the clamp and moves back with the piezo while the inertia of the clamps keeps them stationary, thus completing one step forward. . . . .	30
2.5	Resistor for measuring distance . . . . .	34

2.6	Schematic of cylindrical capacitor for distance measurements. .	35
2.7	Driven scan at different pressures. We can see the signal amplitude increase as the Q increases due to lower pressures. . . . .	37
2.8	Power spectral density at 6 K. This yields $k = 10^{-4}$ N/m at a resonance frequency of 1.4 kHz. . . . .	39
2.9	Single crystal Si cantilever with dimensions of $5 \mu\text{m} \times 400 \mu\text{m} \times 340 \text{ nm}$ . . . . .	39
2.10	Fiber interferometer setup. Light travels from the laser into the 90/10 coupler. 90% of the light is dumped while the other 10% travels towards the cantilever and is reflected back into the coupler. The resulting signal travels through the preamp and into the photodiode to produce a voltage. . . . .	41
2.11	Each complete fringe represents $\lambda/2$ in length. We lock onto the linear region which occurs at $\lambda/4$ [25]. . . . .	43
2.12	Schematic for RF components. . . . .	45
2.13	a) Parallel matched series tuned b) series matched and parallel tuned. . . . .	46
2.14	Artifacts for 20 ms, 50 ms, 100 ms, and 200 ms time constants with the center of each peak marked by a black line. . . . .	49
2.15	Schematic of ultrasensitive cantilever with superconducting annulus . . . . .	53
2.16	Data for z-scan sweep. . . . .	56
3.1	Block diagram of conventional NMR experiment . . . . .	59
3.2	Spin echo centered at 5 ms. . . . .	61
3.3	$H_1$ field strength as a function of distance away from the bottom of the coil. . . . .	61
3.4	Picture of the sample on the cantilever. . . . .	62
3.5	Permalloy magnet field strength as function of distance away from the sample. . . . .	63
3.6	Permalloy magnet gradient field magnitude as function of distance away from the sample. . . . .	64
3.7	1-D scan results with accompanying frequency shift. The $150 \mu\text{m}$ shift is consistent with that expected for the calculated magnetic field distribution due to the field gradient magnet (see text). . . . .	68
3.8	Our resonance slice, in yellow, was only intersects a small portion of the sample due to misalignment between the gradient magnet and sample. . . . .	69

3.9	Spin nutation signal shown across multiple periods. $H_1$ is calculated using $\pi/2 = \gamma H_1 t$ where $\gamma$ is the gyromagnetic ratio and $t$ is the length of the pulse. . . . .	71
3.10	Spin echo centered near 17 $\mu s$ . . . . .	72
3.11	Results from inversion recovery sequence . . . . .	73
4.1	Spin Lattice relaxation measurements of polycrystalline $MgB_2$ at two different fields. Inset: ac susceptibility measurements at various fields [6] . . . . .	76
4.2	$R_s/R_n = (1/T_{1s})/(1/T_{1n})$ v. temperature. A small peak is observed just below $T_c$ [6] . . . . .	77
4.3	Left: quadrupole energy levels and shifts. Right: corresponding resonance lines and arrows showing which transition corresponds to which line. . . . .	79
4.4	1-D scan of $MgB_2$ powder sample with frequency shift to confirm NMR origin of signal . . . . .	83
4.5	Nutation experiment attempt . . . . .	83
5.1	Theoretical structure of 8% doped MnScN where Mn are big red balls, Sc medium sized light blue balls, and N small silver balls [7].	87
5.2	Theoretical $T_C$ 's for different Mn concentration using mean field theory and the cluster variation method. The two green symbols, light colored, use local density approximation and the two black symbols, dark colored, include gap correction. The X symbols indicate the error range. [6] . . . . .	88
5.3	Hysteresis and $M$ v. $T$ curves for nitrogen poor 3% doped Mn. The hysteresis curve was taken at 350 K. . . . .	90
5.4	Hysteresis and $M$ v. $T$ curves for nitrogen poor 15% doped Mn. The hysteresis curve was taken at 340 K. . . . .	91
5.5	MFM image over 1 $\mu m^2$ . . . . .	92
5.6	Hysteresis and $M$ v. $T$ curves for nitrogen rich 3% doped Mn. The hysteresis curve was taken at 350 K. . . . .	93
5.7	Hysteresis and $M$ v. $T$ curves for nitrogen poor 5% doped Mn. The hysteresis curve was taken at 340 K. . . . .	94
5.8	Hysteresis and $M$ v. $T$ curves for 1 % Fe-doped samples. The hysteresis curve was taken at 350 K. . . . .	95

# Chapter 1

## Introduction to Nuclear Magnetic Resonance and Magnetic Resonance Force Microscopy

### 1.1 Basics of magnetic resonance and polarization

Nuclear magnetic resonance (NMR) is a powerful technique whereby manipulating and detecting the evolution of nuclear spins in a sample we are able to learn about the electronic and magnetic structure of the sample.

If we examine a single spin we find that it has a magnetic moment  $\vec{\mu}$  that is proportional to the total angular momentum  $\vec{J}$  through the relation

$$\vec{\mu} = \gamma \vec{J} \quad (1.1)$$

where the proportionality constant  $\gamma$  is the gyromagnetic ratio, which differs for different nuclei. When we subject the magnetic moment to a magnetic field  $\vec{H}$  we observe the Zeeman effect where the magnetic field lifts the energy degeneracy and causes different energy levels to arise depending on the state of the spin. This can be seen by examining the magnetic interaction Hamiltonian  $\mathcal{H}$

$$\mathcal{H} = -\vec{\mu} \cdot \vec{H}. \quad (1.2)$$

If we set the field to be along the  $z$ -axis the Hamiltonian can be rewritten as

$$\mathcal{H} = -\gamma \hbar H_0 I_z. \quad (1.3)$$

The energy eigenvalues of this equation are multiples of  $\gamma\hbar H_0$  where

$$E = -\gamma\hbar H_0 m \quad (1.4)$$

where  $m = I, I - 1, \dots, -I$ .

If we take as an example a nucleus with spin  $I = 1/2$  we find that the two energy solutions are  $1/2$  and  $-1/2$ . If we assume that our nucleus is initially in the lower-energy spin state  $1/2$  and we would like to excite it to the higher energy state we need to bridge the energy gap  $\Delta E$  between the two states where  $\Delta E$  is defined as

$$\Delta E = \hbar\omega \quad (1.5)$$

where  $\omega$  is an angular frequency.

Through the action of an alternating magnetic field that perturbs the Hamiltonian such that only transitions between adjacent levels are allowed we can rewrite  $\Delta E$  as

$$\Delta E = \gamma\hbar H_0 = \hbar\omega \quad (1.6)$$

$$\omega = \gamma H_0 \quad (1.7)$$

This is the condition for inducing a resonant transition between adjacent energy levels. If we know the gyromagnetic ratio of the nuclei and the magnitude of the applied field along the  $z$ -axis then by applying an alternating magnetic field at frequency  $\omega$  we can induce a transition from the lower energy spin state  $1/2$  to the higher energy spin state  $-1/2$ .

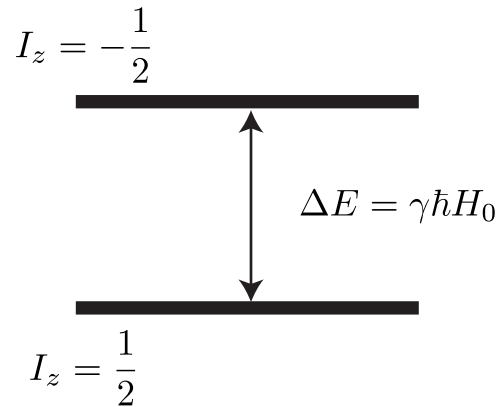


Figure 1.1: Zeeman level splitting for  $I = 1/2$

If we would like to determine the population difference between the two spin states we utilize Boltzmann's distribution yielding

$$\frac{n_{m-1}}{n_m} = e^{-\Delta E/k_B T} \quad (1.8)$$

where  $\Delta E$  is the difference in energy between the two spin states and  $T$  is the temperature [1]. It turns out that the population difference is extremely small at room temperature. For example, for a million protons immersed in a 10 T field at room temperature the population difference between spin up and spin down is only 11 spins. That is an extremely small proportion of spins that actually contribute to the NMR signal. However, NMR as a technique is powerful enough to detect this tiny difference in populations.

In order to determine the magnetization of the sample based on the



applied external field  $H_0$ , the difference in energy,  $\Delta E = \gamma\hbar H_0$ , between the different levels  $m$ , and the total number of spins  $N$  using Eq. 1.4 we can rewrite Boltzmann's distribution in terms of the magnetization of a non-interacting ensemble of nuclear spins  $I$

$$M = N\gamma\hbar \frac{\sum_{m=-I}^I m e^{\gamma\hbar m H_0 / k_B T}}{\sum_{m=-I}^I e^{\gamma\hbar m H_0 / k_B T}}. \quad (1.9)$$

If we take  $\gamma\hbar H_0 / k_B T$  to be a very small number then we can make a linear expansion of the exponential in the above equation to obtain

$$M = \frac{N\gamma^2\hbar^2 H_0}{k_B T} \frac{\sum_{m=-I}^I m^2}{2I+1} \quad (1.10)$$

$$= \frac{N\gamma^2\hbar^2 I(I+1)}{3k_B T} H_0 = \chi_0 H_0 \quad (1.11)$$

where  $\chi_0$  is the susceptibility [2]. This equation is known as Curie's Law and it yields the magnetization for the sample. We note here that Curie's Law utilizes the total number of spins,  $N$ ; however, recall from Boltzmann's distribution that only a small proportion of the spins are polarized and thus manipulated and detected. So while  $N$  is used to calculate the magnetization, only a small portion of these spins contribute to the magnetization.

Another method for performing magnetic resonance experiments relies on the statistical polarization instead of Boltzmann's distribution. Essentially, the statistical polarization states that at any random moment there are fluctuations from the equilibrium polarization on average of  $\sqrt{N}$  [3]. This type

of polarization is best used for NMR studies involving very few spins. If we take for example a sample with  $10^{20}$  spins at room temperature then according to the Boltzmann's distribution there are approximately  $10^{15}$  spins that are aligned. The statistical fluctuation would only have  $10^{10}$  spins polarized; this represents 5 orders of magnitude difference in magnetization. If we now are only interested in a region with 100 spins then we quickly see that the Boltzmann polarization yields on average  $10^{-3}$  spins ,or effectively no net spins that are polarized, while the statistical polarization yields 10 spins. Thus, for extremely high resolution NMR studies it becomes advantageous to utilize the statistical polarization [4] [5]. A side benefit that comes from using the statistical polarization is that there is always another randomly oriented polarization on the order of  $\sqrt{N}$  spins that are aligned and ready to be tipped so you do not have to wait until the spins you have tipped away from the large external field to realign.

## 1.2 Spins in the lab and rotating frame

If we examine the equation of motion of a magnetic moment in the presence of a magnetic field  $\vec{H}$ , we find that the torque is given by

$$\frac{d\vec{J}}{dt} = \vec{\mu} \times \vec{H} \quad (1.12)$$

where  $\vec{J}$  is the angular momentum. Inserting Eq. 1.1 we find that

$$\frac{d\vec{\mu}}{dt} = \vec{\mu} \times (\gamma\vec{H}). \quad (1.13)$$

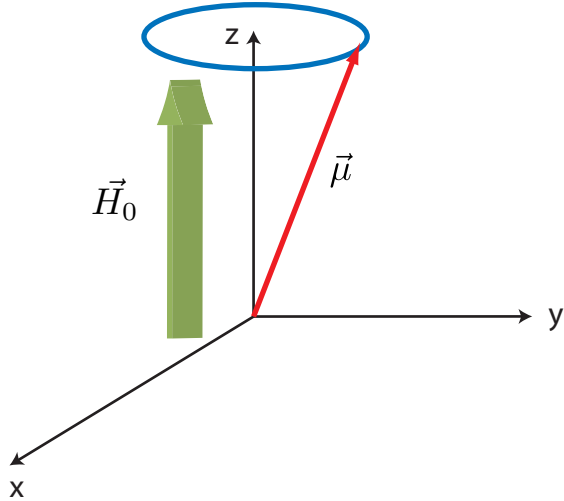


Figure 1.2: Magnetic moment  $\vec{\mu}$  precessing about  $\vec{H}_0$

This equation tells us that the rate of change of the magnetic moment is perpendicular to both the moment itself and the applied magnetic field. Another way to look at it is that if the magnetic field is the polarizing field  $\vec{H}_0$  then the magnetic moment will precess about  $H_0$  in a cone as shown in Fig. 1.2.

Now, what happens when we apply an alternating field  $\vec{H}_1$  perpendicular to the polarizing field  $\vec{H}_0$ ? We can write an alternating magnetic field as

$$\vec{H}_1(t) = H_1(\cos \omega_z t \hat{x} + \sin \omega_z t \hat{y}) \quad (1.14)$$

where  $\omega_z$  is the precession frequency. We now take Eq. 1.13 and add in  $\vec{H}_1$  so that it becomes

$$\frac{d\vec{\mu}}{dt} = \vec{\mu} \times \gamma(\vec{H}_0 + \vec{H}_1(t)). \quad (1.15)$$

We now utilize a useful tool in magnetic resonance and change to a coordinate system rotating about  $\vec{H}_0$  with frequency  $\omega$ , thus, keeping  $\vec{H}_0$  and  $\vec{H}_1$  fixed in this new coordinate system [6]. In order to do so, first take the time derivative of the magnetic moment  $\vec{\mu}$  with respect to time

$$\frac{d\vec{\mu}}{dt} = \frac{\delta\vec{\mu}}{\delta t} + \vec{\omega} \times \vec{\mu} \quad (1.16)$$

where  $\delta\vec{\mu}/\delta t$  represents the rate of change of  $\vec{\mu}$  with respect to the static coordinate system. Then inserting Eq. 1.13 we obtain

$$\frac{\delta\vec{\mu}}{\delta t} + \vec{\omega} \times \vec{\mu} = \vec{\mu} \times \gamma\vec{H}. \quad (1.17)$$

Inserting  $\vec{H}_1$  we get

$$\frac{\delta\vec{\mu}}{\delta t} = \vec{\mu} \times (\vec{\omega} + \gamma\vec{H}_0 + \gamma\vec{H}_1). \quad (1.18)$$

If we fix  $\vec{\mu}$  so it is only along the  $x$ -axis in the rotating frame and note that both  $\vec{\omega}$  and  $\vec{H}_0$  are along the  $z$ -axis then we obtain

$$\frac{\delta\vec{\mu}}{\delta t} = \vec{\mu} \times (\hat{z}'(\omega_z + \gamma H_0) + \gamma H_1 \hat{x}') \quad (1.19)$$

where the  $'$  denotes the rotating frame unit vectors. We now observe that at resonance the  $\hat{z}'$  component goes to zero and recalling that  $\omega_z + \gamma H_0 = 0$  we can substitute  $-\omega$  for  $\omega_z$  thus giving us

$$\frac{\delta\vec{\mu}}{\delta t} = \vec{\mu} \times \gamma \left( (H_0 - \frac{\omega}{\gamma}) \hat{z}' + \gamma H_1 \hat{x}' \right) \quad (1.20)$$

or

$$\frac{\delta\vec{\mu}}{\delta t} = \vec{\mu} \times \vec{H}_{eff}. \quad (1.21)$$

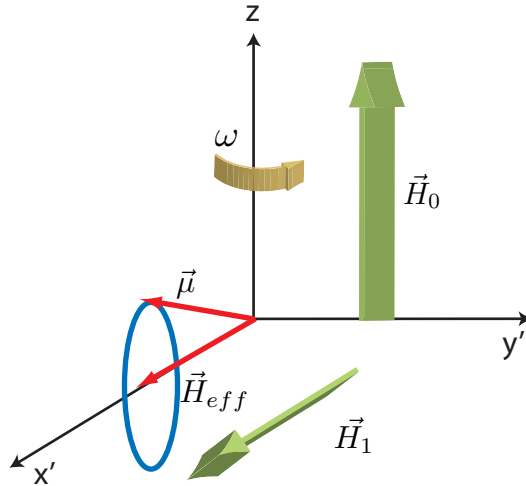


Figure 1.3:  $\vec{\mu}$  rotating about  $\vec{H}_{eff}$  once  $\vec{H}_1$  is applied

$\vec{H}_{eff}$  is the effective magnetic field and  $\vec{\mu}$  will precess about it as shown in Fig. 1.3. We can see that when we apply an alternating magnetic field  $\vec{H}_1$  at resonance ( $\omega = \gamma H_0$ ) only the  $\hat{x}'$  component of  $\vec{H}_1$  survives the special case shown in Fig. 1.3. It is important to note that in NMR experiments the magnitude of  $H_1$  is typically several orders of magnitude smaller than  $H_0$  and by viewing these fields in the rotating frame we can see how it is possible for such a small field to tip the spins away from a much larger field so long as the resonance condition is satisfied.

### 1.3 Spin relaxation

Thus far we have discussed tipping spins without regard to decoherence effects. However, these effects play an important role in the evolution of the

spins and can yield important information on the electronic structure and the internal magnetic field distribution, among many others. We will first examine decoherence in the transverse direction with respect to  $H_0$ , and then in the longitudinal direction.

We will examine the transverse decoherence first through a pulse sequence example. If initially the spins are polarized along  $H_0$  ( $\hat{z}$ ) and we then tip them  $90^\circ$  to the  $x$ - $y$  plane they will precess in the  $x$ - $y$  plane. In a perfect world the spins will precess with perfect coherence, however the presence of magnetic field inhomogeneity causes each spin to experience a slightly different magnetic field, see Fig. 1.4. Since each spin experiences a slightly different magnetic field we can think of each spin as possessing a slightly different resonance frequency, causing the spins to precess at different rates about  $H_0$ . Some spins will precess faster and others will precess slower, and eventually the spins spread out in a fan-like pattern as the spins lose coherence. In order to reestablish coherence after a time  $\tau$  we apply a  $180^\circ$  inversion pulse, i.e. flipping all the spins about the  $x'$  axis. The effect of the inversion pulse is that now the spins that were rotating faster are now behind the spins that are rotating slower, and the spins that were previously rotating slower are ahead. At time  $\tau$  later the spins reform their coherence for a brief time before decoherence takes over again; this is known as a spin echo and is illustrated in Fig 1.4. We can again reform the coherence by applying another  $180^\circ$  pulse. Another spin echo will thus appear, albeit with a decreased amplitude compared to the first one. If you form a train of spin echoes you will find the the amplitude of

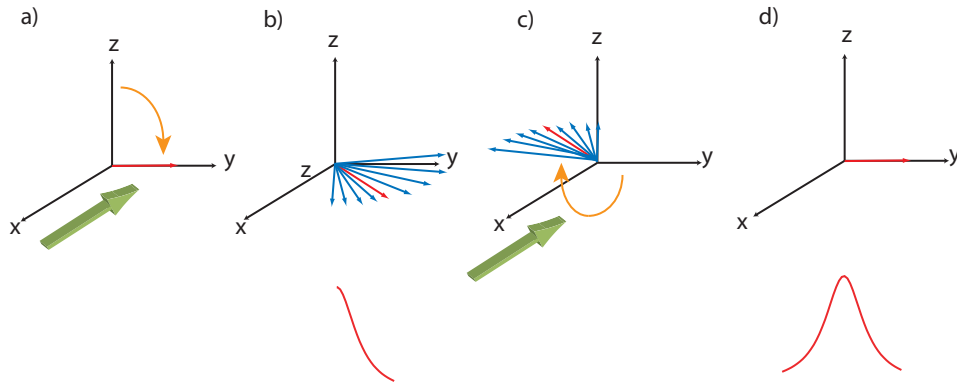


Figure 1.4: a) A  $\pi/2$  pulse rotates the spins  $90^\circ$ ; b) the spins decohere in the transverse plane producing a FID; c) the spins are flipped  $180^\circ$  by a  $\pi$  pulse; and d) the spins reform their coherence resulting in a spin echo.

each echo is a function of the total time  $2\tau$

$$M_1 = M_0 e^{-2\tau/T_2}. \quad (1.22)$$

Equation 1.22 allows you to determine the transverse relaxation times or spin-spin relaxation time,  $T_2$ .

However, we should note that  $T_2$  measures the field distribution the sample experiences and distinguishes whether the inhomogeneity is caused by randomly fluctuating internal fields, known as the homogeneous broadening. One method to measure the total field inhomogeneity due to static inhomogeneous external and internal fields is to examine the decay of an individual spin echo. Each echo decays with a time constant proportional to  $\exp(-t/T_2^*)$ .  $T_2^*$  is a measurement that reflects both the fluctuating and static field distributions that usually correspond to the internal and external magnetic field

inhomogeneities of the sample.

Measuring a different relaxation time in the longitudinal direction, spin-lattice relaxation, can help distinguish between different materials in MRI imaging or determining the pairing symmetry of conduction electrons in a superconductor. When we tip spins in the transverse plane, in addition to losing coherence in the transverse plane, they also tip back towards the external field to reestablish equilibrium. When relaxing back to equilibrium, energy is given up in the process ultimately to the lattice. Interactions with conduction electrons, magnetic ions, and moving nuclear spins often determine the characteristic time  $T_1$  it takes for the spins to realign with the external polarizing field.

Typical methods to measure the spin-lattice relaxation time involve tipping the spins into the transverse plane and then observing how much has recovered longitudinally. In the saturation recovery pulse sequence we use a saturation comb of multiple  $\pi/2$  pulses to randomize the spins creating zero net magnetization. After waiting a variable time  $t$  we apply a  $\pi/2$  pulse to tip the spins back into the longitudinal direction and then induce a spin echo a fixed time later. By varying the time  $t$  between the saturation comb and  $\pi/2$  pulse we find that the echo amplitude decreases according to

$$M(t) = M_0(1 - e^{-t/T_1}). \quad (1.23)$$

Details of spin lattice relaxation in a superconductor will be examined in Chapter 4.



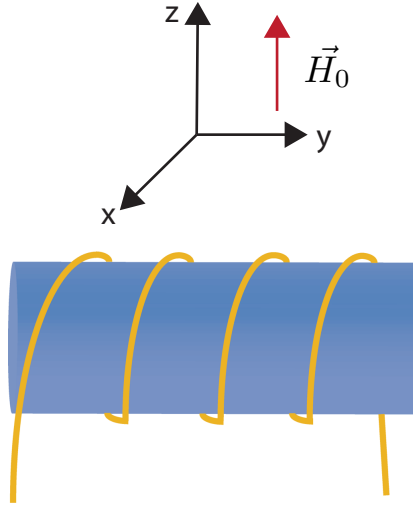


Figure 1.5: Setup for conventional coil NMR.

## 1.4 Experimental setup for conventional NMR

Typical conventional NMR experiments are performed utilizing a setup as shown in Fig. 1.5. The sample is placed in a large magnetic field that produces the polarizing field  $H_0$ . A coil is wrapped around the sample with its axis perpendicular to the polarizing field. RF pulses are sent to the coil at specific time intervals producing  $H_1$  fields to tip the spins. The motion of the spins in the transverse plane is picked up inductively by the coil through Faraday's Law and is sent to a bank of amplifiers and a frequency demodulator to resolve the spin signals. Conventional NMR works well for large samples, but has limitations as we will see below.

## 1.5 Magnetic Resonance Force Microscopy

Magnetic Resonance Force Microscopy (MRFM) was conceived by Sildes as a means to achieve nanoscale spin sensitivity through the combination of scanning probe microscopy (SPM) and NMR/MRI [7]. SPM techniques like atomic force microscopy (AFM) and scanning tunneling microscopy (STM) utilize an extremely sharp tip, down to single atom sharpness in some cases, to achieve atomic scale resolution of a sample surface [8] [9]. However, one of the primary limitations of most SPM techniques is that they are purely surface techniques, unable to probe beneath the surface. MRI on the other hand easily probes beneath the surface of samples as can be readily seen through the MRIs at hospitals that produce 3-D images of a patient. However, current conventional MRI techniques are limited to a sensitivity of approximately  $0.1 \text{ mm}^3$ .

The basic idea behind MRFM involves coupling a mechanical resonator to a magnet producing a large field gradient, [10] [11]. Using Fig. 1.6 as a guide we see that the sample is mounted on an AFM-like cantilever. The motion of the cantilever is detected through a laser fiber interferometer. Parallel to the sample there is a cylindrical magnet that produces a field gradient at the sample. Above the sample there is a RF coil that modulates the magnetization of the sample. Unlike conventional NMR the RF coil in this case does not detect the motion of the spins, for MRFM that is accomplished through the cantilever. The force produced on the cantilever is

$$\vec{F}(t) = (\vec{M}(t) \cdot \vec{\nabla})\vec{B} \quad (1.24)$$

where  $\vec{M}(t)$  is the time varying magnetization of the sample and  $\nabla B$  is the field gradient produced by the magnet. MRFM detection involves the RF manipulating the spins with some time-varying component, and this, in conjunction with the applied field gradient will produce an oscillating force, causing the cantilever to oscillate which is monitored by the laser interferometer.

One of the primary future goals of MRFM is to obtain direct 3-D atomic resolution spin images. Conventional NMR is currently able to determine the structure of some molecules through extremely careful calculations and deductions. In addition to attaining high resolution spin images, the MRFM detection scheme allows it to probe samples where the linewidth has broadened too greatly for conventional NMR to resolve. Another difference is that conventional NMR scans are typically performed by pulsing and then observing the evolution of the spins as a function of time. For instance, the FIDs and spin echoes seen in Fig. 1.4 would show up on the trace of an oscilloscope. MRFM detection differs from conventional NMR in that a RF modulation can be applied to probe the “position” of the spins at one particular increment of time. Through applying the RF modulation pulse at specific time points, MRFM can map out the evolution of the spins as a function of time as in conventional NMR and build up to an image like Fig. 1.4. This has the advantage in that you can probe the spins during the pulse, which is not possible with conventional NMR due to ringing from the amplifier immediately after the pulse that distorts the signal. Probing the spins during the pulse could conceivably allow you to examine  $T_1$  in real time if  $T_1$  is shorter than the RF

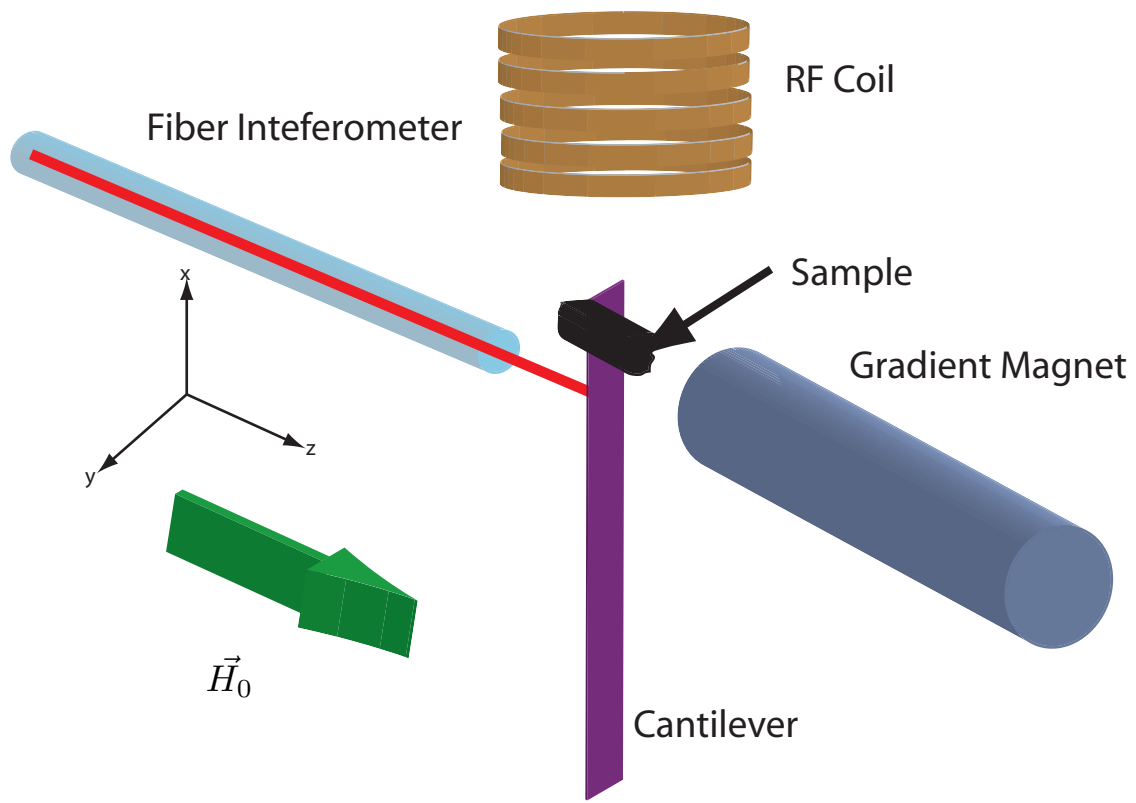


Figure 1.6: Setup for sample-on-oscillator MRFM

pulse length.

## 1.6 Sensitivity of MRFM vs. conventional NMR

Let us compare the detection sensitivity of conventional NMR versus MRFM. Using arguments from Nestle et al. we can write a general signal-to-noise ratio

$$SNR \propto \sqrt{\frac{\omega Q}{k_m T}} \quad (1.25)$$

where  $\omega$  is the operating mechanical oscillator frequency,  $Q$  a general quality factor,  $k_m$  a “magnetic” spring constant, and  $T$  temperature [12]. We will first apply this equation to conventional NMR. We can rewrite Eq. 1.25 using the following definitions

$$k_m = \frac{L}{B_i^2} \quad (1.26)$$

$$Q = \frac{\omega L}{R} \quad (1.27)$$

$$B_i \propto \frac{n}{l} \quad (1.28)$$

$$R \propto \frac{nd}{(l/n)^2} = \frac{n^3 d}{l^2} \quad (1.29)$$

where  $L$  is the inductance of the coil,  $B_i$  the field produced by the coil,  $R$  the resistance,  $n$  the number of turns,  $l/n$  the wire thickness,  $d$  the diameter, and  $l$  the length of the coil. Plugging these terms into Eq. 1.25 we obtain

$$SNR \propto \frac{\omega}{\sqrt{nd}}. \quad (1.30)$$

If we chose to scale down the dimensions of the coil by half, effectively halving the diameter, we find that we gain a  $\sqrt{2}$ x increase in the signal to noise ratio.

Now taking a look at the MRFM case we can write the “magnetic” spring constant as a function of the gradient field  $G$  and the spring constant of the cantilever  $k$  [13]

$$k_m = \frac{k}{G^2}. \quad (1.31)$$

The signal to noise ratio can now be written as

$$SNR \propto \sqrt{\frac{G^2 \omega Q}{kT}}. \quad (1.32)$$

If we scale down the cantilever and halve its spring constant and double the gradient by also decreasing the magnet size, we gain  $2\sqrt{2}$  in signal. We thus see that for the same scaling factor we realize a much larger gain in signal through MRFM versus conventional NMR. Besides this purely theoretical exercise there are several practical reasons why MRFM is more scalable than conventional NMR. In conventional NMR SNR is largely dependent on how much of the volume within the coil is occupied, known commonly as filling factor. For very small coils it becomes very difficult to achieve a high filling factor since the thickness of the wire and sample holder become comparable.

MRFM on the other hand scales quite easily primarily due to the advancement of microfabrication techniques. Making low spring constant cantilevers and small well-defined magnets requires precise control of silicon etching and metal deposition processes. Since these techniques have been more or less consistent with Moore’s Law there appears to be ample room for scaling. The answer to the question of whether single nuclear spin resolution can

be achieved becomes one of when, not if (though it appears that the current generation of MRFM detection techniques may not be the answer).

The magnetization from the spins is derived from Curie's law and thus Eq. 1.24 can be rewritten as

$$F = \frac{N\gamma^2\hbar^2 I(I+1)}{3k_B T} H_0 \nabla H \quad (1.33)$$

where  $I$  is the spin quantum number. The minimum detectable force is

$$F = \sqrt{\frac{4kk_B T \Delta\nu}{\omega Q}} \quad (1.34)$$

where  $k$  is the spring constant,  $\Delta\nu = 1/4\tau_c$  is the detection bandwidth with time constant  $\tau_c$ ,  $\omega$  the cantilever frequency, and  $Q$  the quality factor of the cantilever.

Examining this equation there appear several routes to high detection sensitivity. The temperature is the easiest to manipulate since it involves the use of cryogenics. Designing cantilevers with low spring constants and high quality factors is crucial although current micro-electro-mechanical (MEMS) fabrication techniques and physical limitations constrain them to values around  $k = 10^{-5}$  N/m and  $Q = 10^6$ , respectively. The cantilever frequency cannot be raised significantly since that would violate the adiabatic condition and the detection bandwidth is limited to certain values due to noise washing out the signal at small time constants.

## 1.7 Cyclic adiabatic inversion

One of the crucial aspects of MRFM to realize a strong signal is to bridge the large gap in resonance frequency between the spins and cantilever. In typical NMR experiments the spins are precessing at several hundred MHz while a typical cantilever has a resonance frequency of only a few kHz. We must transfer the motion of the quickly precessing spins to the relatively slow oscillating cantilever. The technique we use to bridge the resonance frequency gap is a type of repeated adiabatic rapid passage known as cyclic adiabatic inversion (CAI), see Fig. 1.7 [14]. Initially, the spins are off-resonance precessing about the static magnetic field  $H_0$ . We then apply a field from the RF coil that starts off-resonance and then brings the spins to resonance ( $x' - y'$  plane in the rotating frame). Once at resonance we modulate the RF field about the resonance frequency with a modulation frequency that is equal to the cantilever's resonance frequency. The effective field can be written as

$$\vec{H}_{eff} = \frac{\Omega}{\gamma} \cos(\omega_{osc}t) \hat{z} + H_1 \hat{x}' \quad (1.35)$$

where  $\Omega$  is the modulation depth. The modulation about the resonance frequency creates a time varying magnetization resulting in a time varying force causing the cantilever to vibrate. The frequency modulation also ensures this force occurs at the cantilever resonance frequency, thus significantly enhancing the cantilever response.

Since CAI is an adiabatic process a restriction exists in that the modulation must be done “slowly enough” that we don't lose the spins. If we



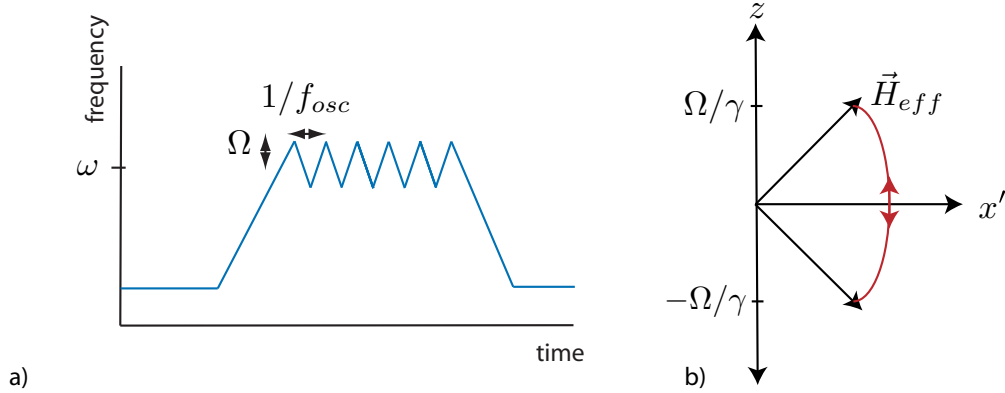


Figure 1.7: a) cyclic adiabatic inversion with amplitude  $\Omega$  and frequency  $1/\omega_{osc}$  about the resonance field  $\omega$ . b) In the lab frame the spins move above and below the transverse plane with amplitude  $\Omega$ .

modulate too quickly the spins will not follow the effective field  $H_{eff}$  and the magnetization will not be modulated. The condition for how fast we can modulate the spins can be written as

$$\Omega \ll \frac{(\gamma B_1)^2}{\omega_{osc}}. \quad (1.36)$$

Miller examined what exactly  $\ll$  meant and through a systematic study where he changed  $\Omega$  and from the resulting signal he found that  $\ll$  meant roughly 6 [15].

CAI for MRFM only allows measurement of spins along the longitudinal direction, a direct contrast to coil NMR which is sensitive to the transverse direction. In addition, CAI usually only allows you to measure the magnetization at a specific time unlike coil NMR where you can observe the evolution of the spins across time. Thus adapting pulse sequences developed for coil

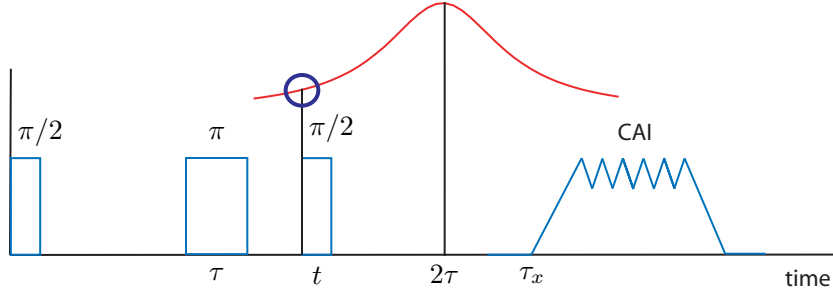


Figure 1.8:  $\pi/2-\tau-\pi-t-\pi/2-\tau_x$ -CAI where  $\tau_x$  is varied to obtain the spin echo. The spin echo is shown above where the center occurs at  $2\tau$ . From this plot we can see that by choosing  $t$  smaller than  $\tau$  we have obtained a point on the spin echo far from its peak.

NMR requires we add an additional CAI pulse after the coil NMR sequence as well as varying the times at which we apply the CAI pulse. For example, in the spin echo pulse sequence described previously we utilized  $\pi/2-\tau-\pi$ . For MRFM we would modify this sequence to  $\pi/2-\tau-\pi-t-\pi/2-\tau_x$ -CAI, see Fig. 1.8. The additional  $\pi/2$  pulse tips the spins back into the longitudinal direction so the spins will be detectable for MRFM. We then wait a time  $\tau_x$  before applying a CAI pulse to sample the magnetization. In order to map out the spin echo we essentially start with a  $t$  smaller than  $\tau$  and end with a value greater than  $\tau$ ; essentially the width of the spin echo will determine the width of the magnetic field distribution.

## 1.8 Resonance slice and imaging

The high resolution capabilities of MRFM are derived primarily from the high field gradient from a nearby magnet. We can think of the gradient splitting up space into thin volume slices where the magnetic field is essentially constant and the resonance condition for only one magnetic field is satisfied. The geometry of these thin volume slices are modified by  $\Omega$  since the spins are modulated about the resonance through CAI. We can then define the thickness of these slices as

$$\Delta z = \frac{2\Omega}{\gamma \nabla B} \quad (1.37)$$

commonly termed the resonance slice. We can tune the resonance slice to nanoscale dimensions primarily by increasing the field gradient. If we are detecting protons with a field gradient of  $10^6$  T/m then we can reach a resonance slice width of approximately 4 nm. Imaging in conventional NMR and MRI is also done using a gradient and resonance slices, but such slices tend to be much larger due to the size of the gradient magnets used, and more importantly their signal resolution limits them to large slices with many spins providing a large signal.

Imaging with the presence of the resonance slice requires that we know the magnetic field profile of the gradient magnet. We must determine what part of the sample is intersected by the resonance slice in order to determine the spin contribution from that part of the sample. We can thus rewrite the

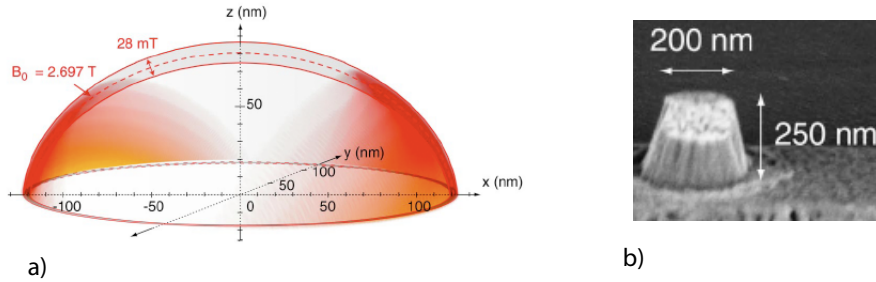


Figure 1.9: a) Resonance slice shape for a magnet with shape. b). Notice that the thickness of the slice is not constant and depends on the position. Equation 1.37 applies only for one particular point in space that has a particular field gradient [23].

force equation as

$$F_z = \int_V dx^3 M_z(x) \partial_z B_z \quad (1.38)$$

[17]. We must determine the field profile for the gradient magnet based on its geometry and distance from the sample. The field profile tells us the shape of the resonance slice and from it we can take the force data and deconvolute it to obtain an image. An example is shown in Fig. 1.9.

## Chapter 2

# Experimental details of magnetic resonance force microscopy

### 2.1 He-3 cryostat

Our microscope is mounted at the base of an Oxford Heliox VL cryostat. The cryostat is designed to reach a base temperature of 300 mK using helium-3. The vacuum can for the probe is affixed using vacuum grease and the inner vacuum chamber (IVC) must be pumped out immediately after it is placed onto the cryostat to avoid slippage. Detailed instructions for low temperature operation is given in the Heliox manual so we will only discuss the basic concepts of its operation.

Generation of the base temperature occurs in two steps. Helium-4 is drawn into the 1 K pot through the needle valve which is then pumped on, reducing the vapor pressure above the liquid and removing heat. The temperature in the 1 K pot then drops to around 1.5 K through evaporative cooling. With the 1 K pot at its base temperature, the sorb in the charcoal in the He-3 space is heated to 30 K releasing the He-3 gas. The helium-3 gas liquefies and flows past the 1 K pot down to the helium-3 pot. The helium-3 pot is then pumped on by cooling the same sorb and the base temperature of

300 mK is reached shortly thereafter.

Wiring used in the probe consisted of Ni clad-coated copper wires and Lakeshore low temperature coaxial cables (CC-SS and CC-C) for RF cabling. It is essential that all wiring is heatsunk at both the 1 K pot and He-3 pot. Originally, the RF wire was conventional RG-154, however the thickness of the wire and material type brought a large amount of heat into the probehead preventing the attainment of the base temperature. The wire feedthroughs at the top of the probe were sealed with 1266 Stycast epoxy. Several layers of Stycast should be carefully applied in order to ensure against any vacuum leaks.

## 2.2 Probehead

The probehead consists of two pairs of Attocube-type stages to position the fiber interferometer with respect to the micro-oscillator and the gradient magnet relative to the sample and a copper plate that holds the cantilever and the RF board, Fig. 2.1.

The cantilever holder consists of a bronze clip and a disk piezo that can actuate the cantilever at various frequencies, see Fig. 2.22 The RF board is affixed to the copper plate through an insulating nylon plate. The entire probehead is mounted at the base of the helium-3 pot.

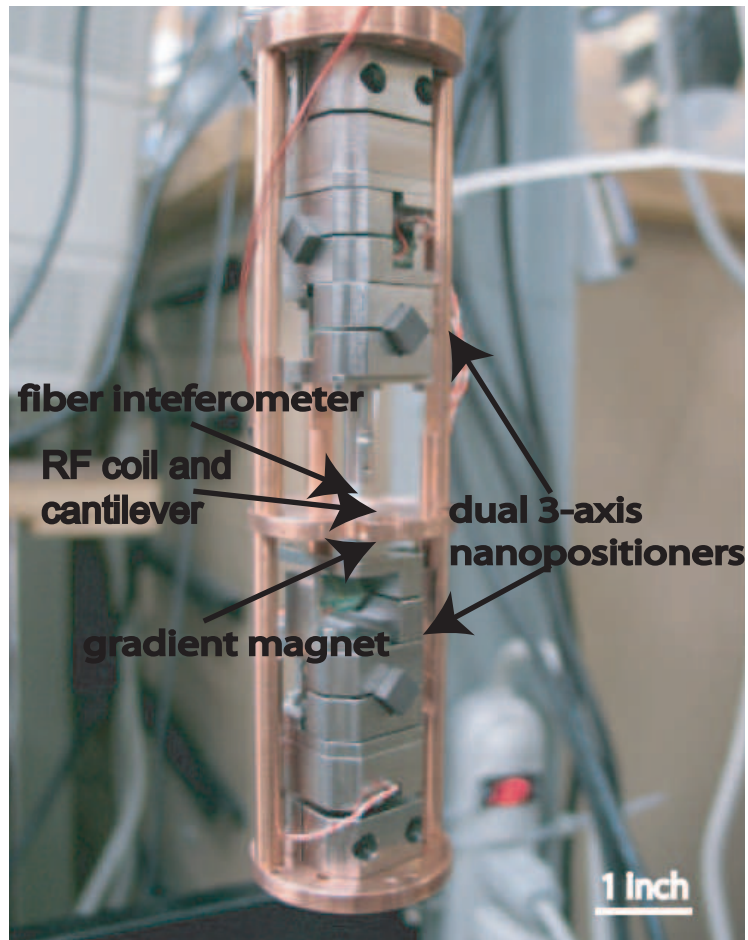


Figure 2.1: Microscope head of the He-3 probe

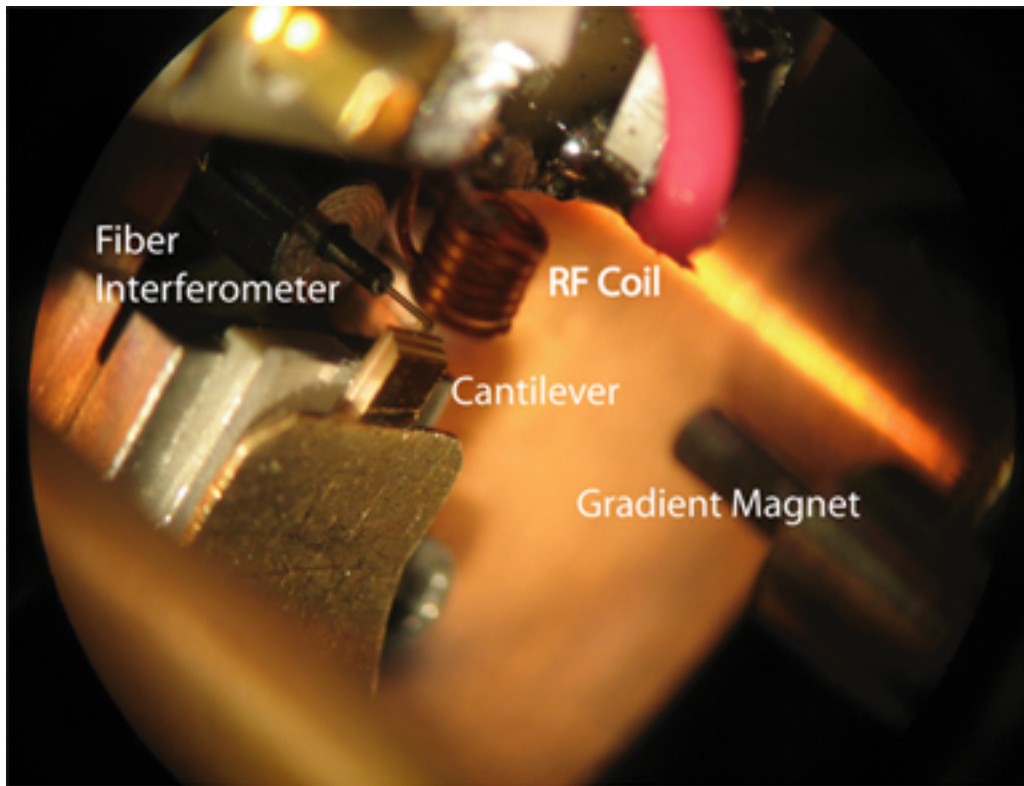


Figure 2.2: Blow up of the microscope head



### 2.3 Attocube-type positioners

The Attocube-type stages are stick-slip type stages with coarse motion over several millimeters and finer motion down to the sub-nanometer level. The Attocube-type stages consist of a 3.5 mm x 4.5 mm x 10 mm stack piezo that is epoxied with Epotek H77 black epoxy to a 10 mm long graphite rod. This combination is then epoxied to a base plate on the piezo face end. The graphite end is then clamped by two pieces where the clamping force is adjusted by two 2-56 screws with a spring underneath each screw, see Fig. 2.3.

The plate and the two clamping pieces are machined out of titanium since it is lightweight and non-magnetic. A sawtooth wave is then sent to the piezo as shown in Fig. 2.4. The reason we require the sawtooth shape to induce motion is because when the voltage ramps up slowly the piezo expands sliding the graphite forward with the attached clamp, the stick phase. The rod was chosen to be graphite because it acts as a lubricant that also allows for a sliding motion. The voltage is then rapidly brought to zero and the piezo contracts, the slip phase. However, since little friction from the clamp is holding the graphite, it slips and we maintain the forward progress achieved during the stick phase. Through a series of waveforms we can transverse large distances in a step by step manner. A typical step size at room temperature is approximately 3  $\mu\text{m}$  while at low temperatures this is reduced to 1  $\mu\text{m}$ .

There are several important considerations when using the Attocube-type positioners. The most important one is that the motion between the positive and negative directions is not always linear. At some positions each

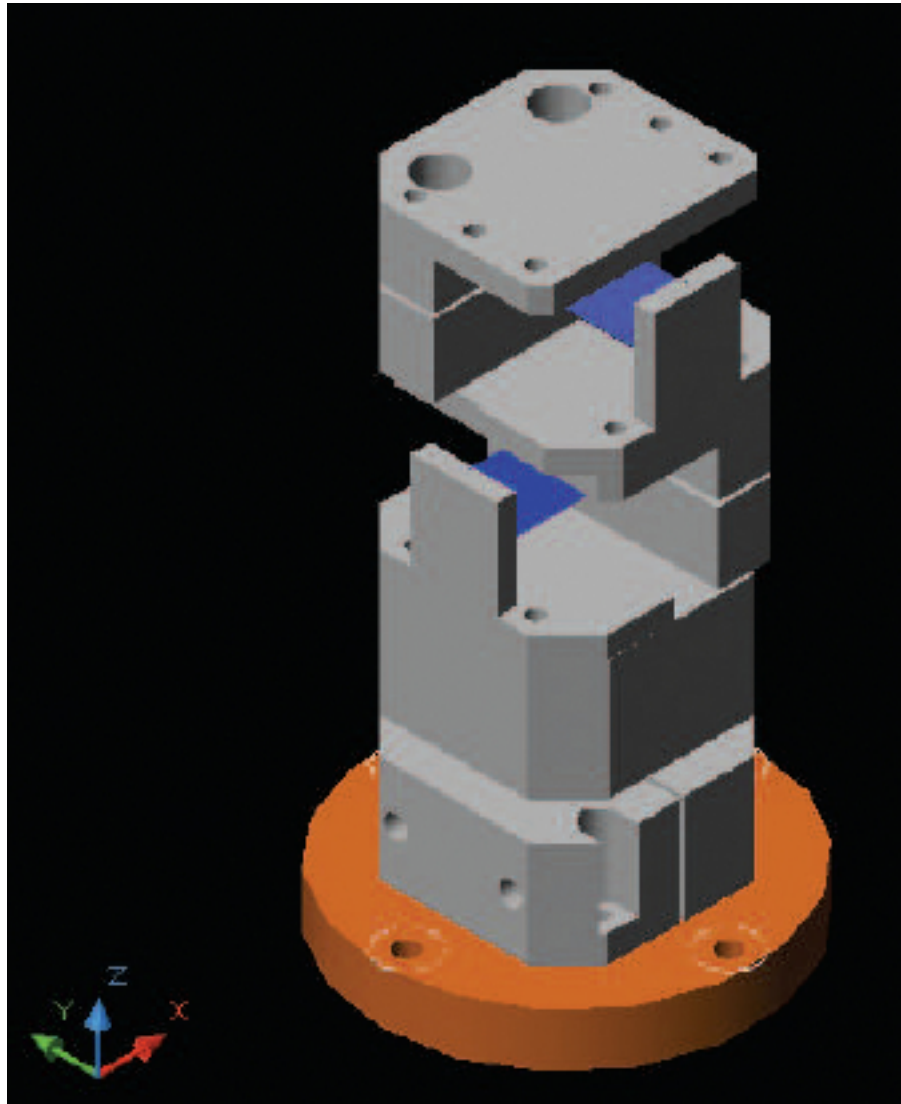


Figure 2.3: 3-D CAD drawing of Attocube stages [18]

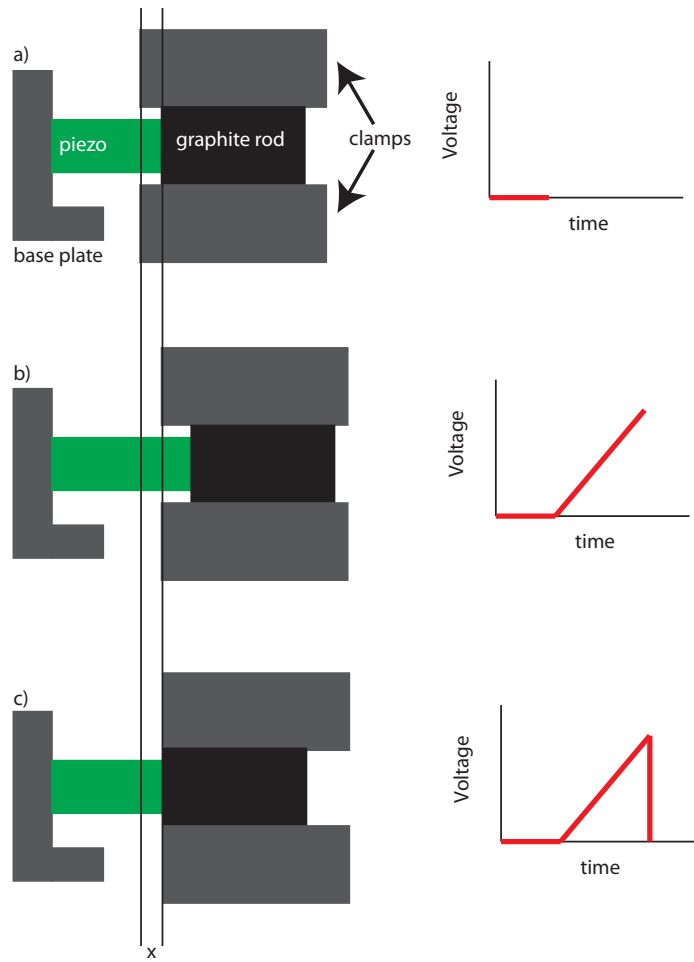


Figure 2.4: a) Initial state of the stage, b) The piezo is slowly expanded by a rising voltage causing the clamp and graphite rod to move forward as well. c) The voltage applied to the piezo is rapidly ramped to zero causing the piezo to retract. The graphite rod “slips” within the clamp and moves back with the piezo while the inertia of the clamps keeps them stationary, thus completing one step forward.

sawtooth wave produces a larger or smaller step. It may not seem obvious that non-linearity would exist based upon the design of the stages, but we suspect that it is due to imperfections on the interface between the graphite rod and the two clamping pieces. The surface roughness of the two clamping pieces and graphite rod is not uniform so we can imagine that at some areas the friction is higher than in others. The non-uniformity of surface roughness can cause movement that deviates as much as 100% between one position and another.

The other consideration with the Attocube-type stages is how tight we should clamp the graphite rod. Since MRFM experiments are run at high magnetic fields and the titanium in the stages are not 100% non-magnetic, the  $z$ -stages tend to slip downward. This can have unintended consequences such as the fiber crashing into the cantilever or the gradient magnet being in a position we did not expect. The simple solution is to tighten the screws in the two clamping pieces to prevent slippage. However, there is a compromise in that we must now use a much higher voltage sawtooth wave to actuate the stages. At low temperatures where high voltages are already needed to induce movement and given that the piezos have a maximum voltage input of 150 V, it becomes very difficult to actuate the stages with very high clamping forces at low temperature. What we do is, in effect, compromise by allowing a little slippage in the  $z$ -stages while enabling movement at low temperatures. In order to prevent the fiber from crashing into the cantilever we apply feedback to control the fiber-cantilever distance. As for the gradient magnet, we monitor

its position as we will discuss in the next section.

The primary advantage of the Attocube is its ability to traverse large distances quickly and allow us to position the fiber as well as the gradient magnet with respect to the cantilever quickly. However, the cost of this convenience is that the Attocubes tend to slip and vibrate. For example, after we have aligned the fiber and cantilever in air, we affix the vacuum can to pump out the IVC. The vibration induced in this action can cause the Attocubes to slip, thus losing fiber to cantilever alignment. Re-aligning them is not too difficult with some practice, however it can become a nuisance when a stage moves in unpredictable directions. An alternate design would have been to affix the fiber to a permanent structure with respect to the cantilever preventing any type of movement. However, the price of this design is that it can take a long time to align them initially since precise positioners are typically not available and adjustments can only be made *ex situ*, no adjustments can be made under vacuum and at low temperatures. For most of the experiments described in this dissertation the Attocubes are adequate, but for more sensitive experiments where limited spurious movement between the fiber and cantilever caused by thermal fluctuations or vibrations is required, an alternate design may be more preferable.

## 2.4 Capacitor position sensor

Due to the step size non-linearity of the Attocubes it was essential to utilize some sort of sensor to determine exactly how much distance the stages

had traversed. Initially we used an interferometer to measure the step size by observing the number of steps it took to traverse a fringe. However, this technique often gave us false readings because when calibrating for small step sizes sometimes the stages seemed to be oscillating about a point instead of moving in just one direction thus giving us the impression that it was traversing a fringe when in fact it was just going back and forth across the same fringe. The other problem with the interferometer is that we could not measure the distance when performing an experiment because repositioning the fiber to shine on the stages and then back to the cantilever is a risky process that usually results in us not having any idea where the fiber is.

Given the limitations of interferometric detection we utilized resistive detection as the next technique. The resistor itself is a linear potentiometer that measures resistance depending on its position on a sliding stick, see Fig. 2.5. We affixed the resistor to the top plate of our  $z$ -stage and achieved a resolution of around  $1 \Omega/\mu\text{m}$ . This setup works very well at room temperature since it enabled us to directly measure the position of the gradient magnet. However, at low temperatures it becomes difficult to use because it adds an additional frictional force that must be overcome to induce motion. At low temperatures the movement of the stage is already marginal and adding the resistor made movement much more difficult.

Thus our solution was to use capacitive detection due to its frictionless operation and high sensitivity [19]. The design we employ is a cylindrical capacitor with a small gap between the two pieces, Fig. 2.6. The capacitance



Figure 2.5: Resistor for measuring distance

for a cylindrical capacitor is defined as

$$C = 2\pi\epsilon_0 \frac{L}{\ln(b/a)} \quad (2.1)$$

where  $\epsilon_0 = 8.85 \text{ pF/m}$  in air,  $L$  is the length of the capacitor, and  $b$  and  $a$  are the diameters of the outer and inner conductors, respectively. We chose OFHC copper as the material and the dimensions are approximately  $L = 10 \text{ mm}$ ,  $b = 4 \text{ mm}$ , and  $a = 3.9 \text{ mm}$ . We thus obtain a total predicted capacitance of  $21.9521 \text{ pF}$ . Now say that we want to vary the length by  $10 \mu\text{m}$ , we then obtain a capacitance of  $21.9302 \text{ pF}$  a difference of  $0.0219 \text{ pF}$ . In order to measure such a small capacitance change we initially used a capacitance bridge where the capacitance was measured through a null voltage using lock-in detection. Unfortunately the bridge we had in the lab was old and not very accurate yielding different results each time it was used. Then fortuitously a former colleague informed us that a chip had been developed by Analog Devices which converts an analog capacitance signal into a digital signal that can be read on a computer. We purchased the EVAL-AD7746BZ board and it enables resolution down to  $10^{-6} \text{ pF}$  which allows us to reach nanometer

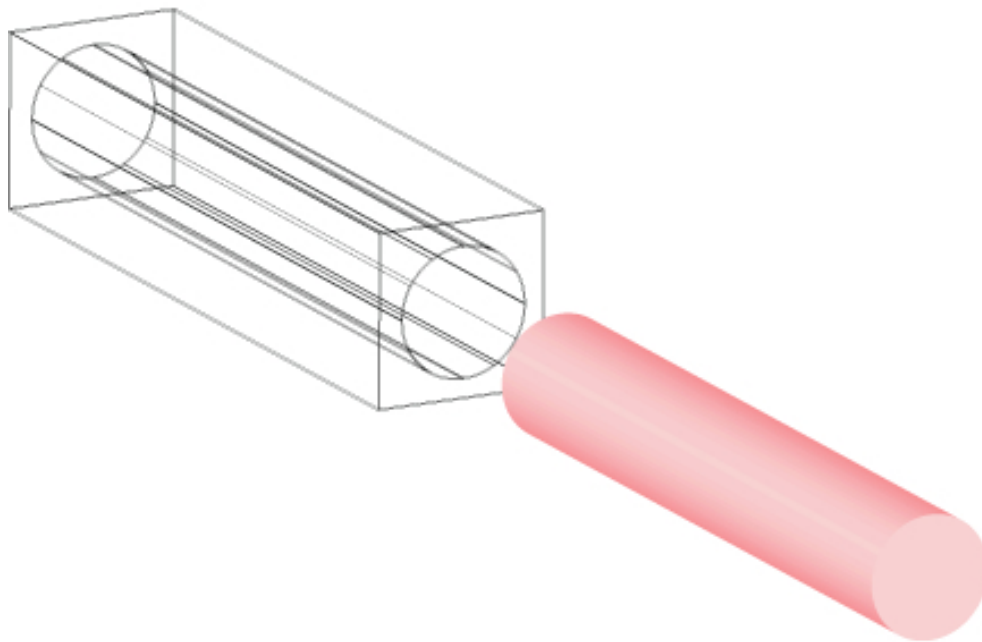


Figure 2.6: Schematic of cylindrical capacitor for distance measurements.

resolution. Some signal averaging is required to sharpen the resolution, but we have observed a resolution down to 300 nm. This is quite a bit larger than the predicted resolution of 1 nm and most of this is due to poor connections between the coaxial cable in the probe and the wires on the capacitor as well as electrical noise. Despite the relatively poor resolution, it is more than sufficient for most of our scanning needs.

## 2.5 Cantilevers

Ideally for NMRFM we prefer cantilevers with low spring constant, high  $Q$ , and low resonance frequency. Low spring constant and high  $Q$  cantilevers



contribute to higher force resolution. However, we should note that extremely high Q's can make the experiment more difficult due to RF heating of the cantilevers causing the resonance peak to shift. In order to work around this problem active feedback can be utilized to artificially damp the Q while keeping the actual Q the same [20]. As for the resonance frequency, ideally it would be as high as possible to enhance the force resolution. However, we need to obey the adiabatic condition and so this usually limits us to resonance frequencies of roughly 5 kHz or less.

In order to maximize the force resolution of our cantilevers we utilize a bar geometry with a pad for loading samples onto. The resonance frequency and spring constant of a thin bar cantilever ( $t \ll w$ ) can be written as

$$k = \frac{1.03}{4} E \frac{wt^3}{l^3} \quad (2.2)$$

$$f = \frac{3.516}{2\pi} \left( \frac{E}{12\rho} \right)^{1/2} \frac{t}{l^2} \quad (2.3)$$

where  $w$  is the width,  $t$  the thickness,  $l$  the length,  $E$  the Young's modulus, and  $\rho$  the density of the cantilever [21]. Examining these equations shows that making long, thin cantilevers yields the lowest spring constant.

We commonly employ two methods to characterize the cantilever, either a frequency sweep or a noise scan. In the frequency sweep we drive the cantilever at specific frequencies using the disk piezo and measure the AC amplitude of the cantilever at each frequency. Fig. 2.7 shows a typical frequency sweep scan. The frequency sweep method is a quick and easy-to-use method to determine the resonance frequency and Q. The shape of the lorentzian helps

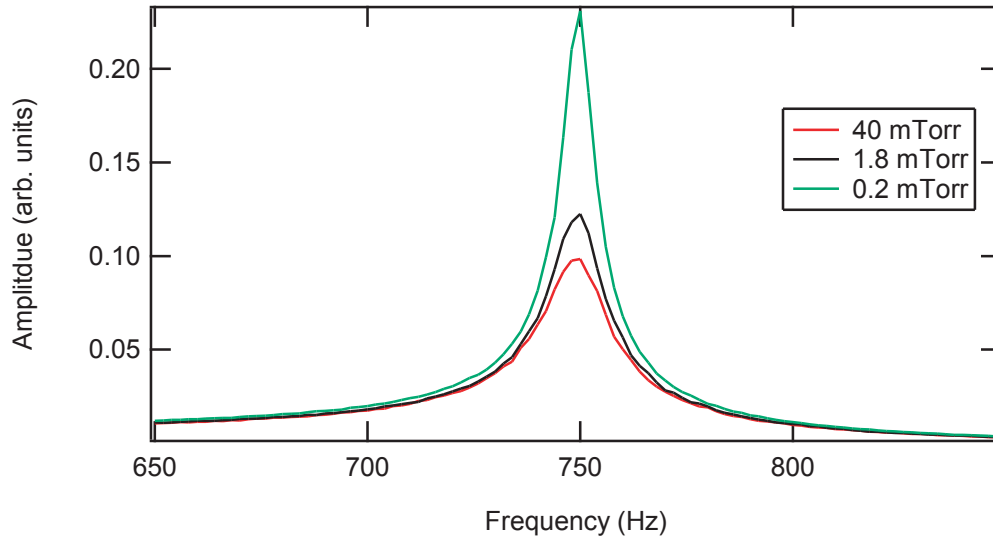


Figure 2.7: Driven scan at different pressures. We can see the signal amplitude increase as the Q increases due to lower pressures.

to determine whether the cantilever has incurred any damage such as running epoxy or opening frictional cracks.

Typically, we perform the frequency sweep at the highest possible drive amplitude (although not exceeding 1 V) to obtain the best possible signal. However, sometimes the response of the cantilever is extremely strong and it is necessary to either decrease the drive amplitude or increase the lock-in sensitivity to obtain an accurate signal.

Noise scans enable us to determine not only the resonance frequency and Q of the cantilever, but the spring constant as well. The equipartation theorem states that

$$\frac{1}{2}k \langle x^2 \rangle = \frac{1}{2}k_B T \quad (2.4)$$

where  $\langle x^2 \rangle$  is proportional to the spectral density of the oscillator [22]. In a noise scan we perform a time domain scan of the cantilever without any outside actuation and then perform a Fourier transform to obtain the frequency spectrum. First we tell the lock-in to look at the amplitude of the cantilever in a range of frequencies about the guessed resonance frequency for several seconds. This time series data will look like random noise. However, when we Fourier transform the squared voltage signal we obtain the frequency response of the cantilever. Fig. 2.8 shows a typical Fourier transformed noise scan of the cantilever described in Fig. 2.9. The frequency resolution is set by the bandwidth of the lock-in measurement. The lock-in can only store 16,384 points in its buffer, so a larger bandwidth will restrict the frequency resolution.

Once we have obtained the spectral density we need to convert this value to amplitude

$$\langle x^2 \rangle = \left( \frac{\lambda}{2\pi V_{pp}} \right)^2 V^2 \quad (2.5)$$

where  $\lambda$  is the wavelength of the laser,  $V^2$  is the square of the signal amplitude, and  $V_{pp}$  is the peak to peak voltage of the interference fringe. This converts the spectral density from units of volts squared to meters squared. We then utilize Eq. 2.4 to obtain the spring constant.

Conversely, if we already measured the spring constant we can use a noise scan to determine the temperature of the cantilever. This is important in low temperature measurements since the thermometer is located on the copper plate to which the cantilever is affixed to and not directly on the cantilever. Thus the noise scan is the most accurate way to determine the cantilever

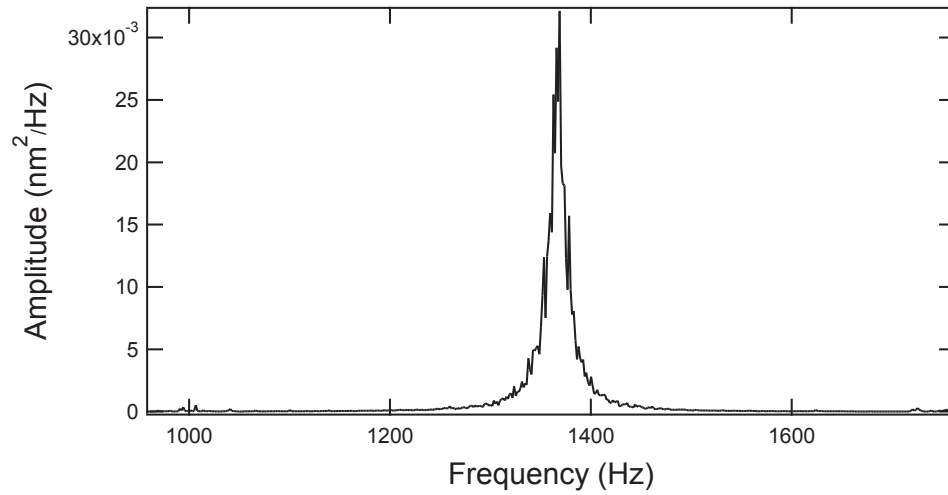


Figure 2.8: Power spectral density at 6 K. This yields  $k = 10^{-4}$  N/m at a resonance frequency of 1.4 kHz.

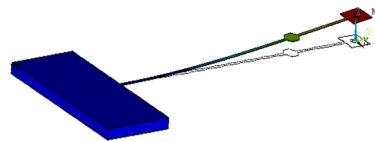


Figure 2.9: Single crystal Si cantilever with dimensions of  $5 \mu\text{m} \times 400 \mu\text{m} \times 340 \text{ nm}$ .

temperature, an important consideration for SNR calculations and samples that undergo phase transitions at particular temperatures. However, while a noise scan is an accurate method to determine the temperature or spring constant it is not a precise method. In our experience we typically see a standard deviation of roughly 10%. Some of the reasons for the cause of this lack of precision is electronic noise in the detection and unstable vibrations the cantilever experiences. Thus we interpret the noise scan measurements to yield good accuracy but poor precision thus giving us only ballpark estimates of the spring constant and temperature.

## 2.6 Fiber interferometer

In order to read out the motion of the cantilever we utilize an infrared fiber interferometer [23]. The interferometer is advantageous in that it is compact and produces minimal low frequency noise. The schematic for our interferometry setup is shown in Fig. 2.10. A 1550 nm laser is used as our light source and it travels down path 1 into the directional coupler. Previously, the lab had used visible red lasers, but they were found to cause heating of the cantilever since the wavelength bridges the bandgap of silicon [24]. The light is split into a 90/10 ratio, with the 90% portion traveling down path 2 and the 10% portion traveling down path 3 towards the cantilever. The reason the 90% portion is not used to detect the cantilever is because it results in extra radiation heating of the cantilever. For the portion traveling down path 3, 96% of the light intensity travels towards the cantilever, while 4% is reflected

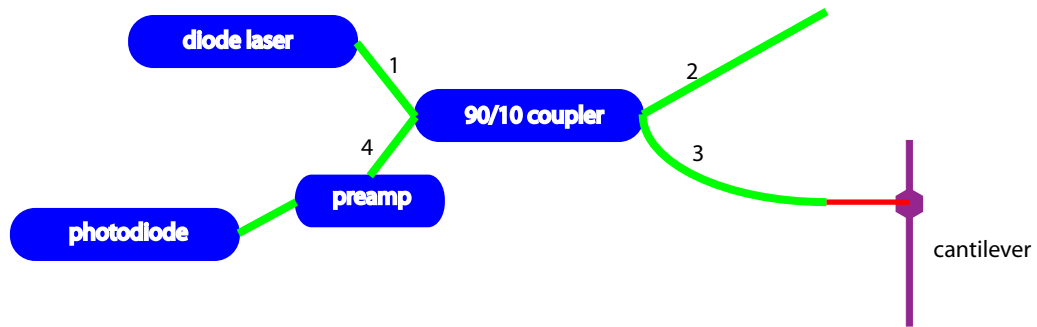


Figure 2.10: Fiber interferometer setup. Light travels from the laser into the 90/10 coupler. 90% of the light is dumped while the other 10% travels towards the cantilever and is reflected back into the coupler. The resulting signal travels through the preamp and into the photodiode to produce a voltage.

back into the coupler due to the ratio of the index of refraction of glass with respect to air. The light exiting the fiber reflects off the cantilever and much of it travels back into path 3. The cleaved end of the fiber is typically placed approximately  $50 \mu\text{m}$  or less from the cantilever in order to maximize the signal reflecting back into the fiber. The two reflected light waves interfere and a fraction of it is sent down path 4 to the photodiode. The light is converted to a current by the photodiode and the current is then converted into a voltage by an op-amp circuit.

It is important to note that the photodiode signal consists of an AC and DC component. The DC component is measured by a voltmeter and is related

to the distance between fiber and cantilever (assuming all of the laser light is incident on the cantilever). By adjusting the fiber-cantilever distance we will see fringes appear as shown in Fig. 2.11. The peak-to-peak distance represents a movement of distance  $\lambda/2$ . While running experiments we would like to keep the fiber to cantilever distance fixed for DC. We thus use a simple feedback circuit, details of which can be found in Yong Lee's thesis, which varies the voltage of the  $z$ -piezo stack from 0 to 36 V in the fiber Attocube so that the fiber-cantilever distance remains constant for DC. The point on the fringe that we hope to stay on is in the middle since it yields the highest sensitivity and its linearity ensures a constant sensitivity over the largest range.

The AC part of the photodiode signal represents the oscillation of the cantilever. Here you might ask how that is possible if the DC part is keeping the fiber-cantilever distance constant, wouldn't that always result in a net oscillation amplitude of zero? The key to resolving this dilemma is realizing that typical cantilever resonance frequencies are in the kilohertz range while our DC feedback is done typically only below 200 Hz. Thus the DC feedback only keeps the fiber-cantilever distance constant at low frequencies and does not affect or detect higher frequency oscillations by the cantilever. We can thus think of the AC signal as oscillating about the midpoint of the fringe.

## 2.7 RF circuitry

In order to generate radiofrequency fields we utilize a small coil which we wrap by hand about either a pipette or resistor leg. The magnetic field of

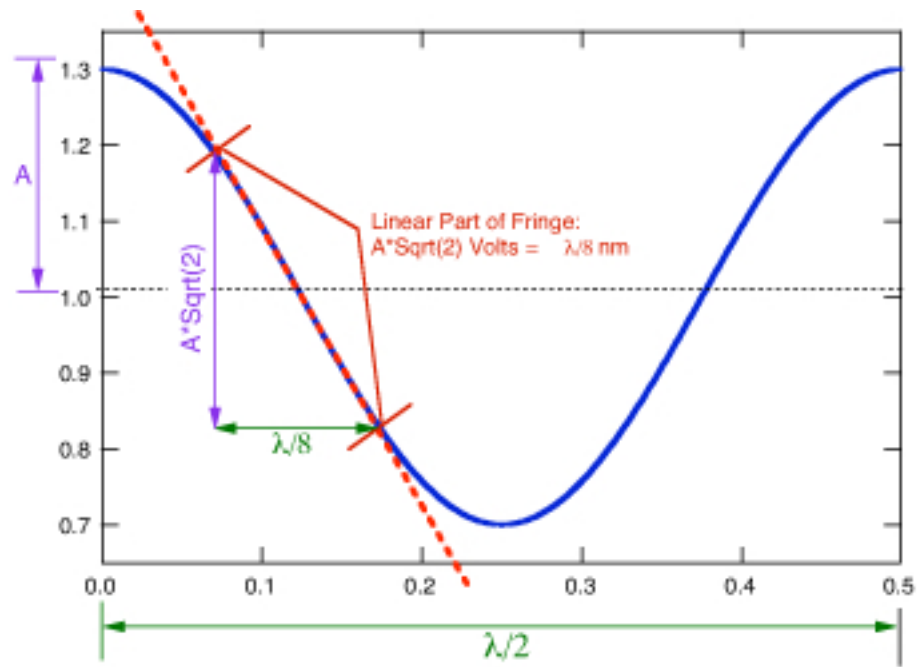


Figure 2.11: Each complete fringe represents  $\lambda/2$  in length. We lock onto the linear region which occurs at  $\lambda/4$  [25].



a coil is defined as

$$B = \frac{1}{2} \mu_0 \frac{N}{L} I \left[ \frac{z_0}{\sqrt{z_0^2 + R^2}} - \frac{z_0 - L}{\sqrt{(z_0 - L)^2 + R^2}} \right] \quad (2.6)$$

where  $N$  is the number of turns,  $L$  the length,  $I$  the current,  $z_0$  the distance  $z$  outside the coil measured along the axis from the middle of the top turn, and  $R$  the radius of the coil [26]. In order to maximize the field generated by the coil, we wrap coils with a few turns, a small radii and use as much current as possible. Our coils are made from Ni clad coated copper wire; the Ni clad coating is an insulating coating that prevents shorts between the individual turns. The coils we used were 3.5 turns with inner diameters of 800  $\mu\text{m}$  and 1700  $\mu\text{m}$ .

In order to deliver maximum power from the RF power amplifier to the coil we must utilize a tuned, or impedance matched, network. We achieve this by using tuning capacitors that can change the overall impedance of the circuit. The circuit diagram for our RF circuit is shown in Fig. 2.12. The capacitors are located outside of the probe separated by a long coaxial cable (Lakeshore CC-C-50 due to its low thermal conductivity). Ideally, the capacitors would be located closer to the coil to ensure better tuning, however it becomes difficult to tune at low temperatures since we cannot access the tuning capacitors when the IVC is sealed.

The tuning capacitors are either parallel tuned series matched, or series tuned parallel matched as shown in Fig. 2.13. Ultimately, the configuration we chose to use was the one that tuned to the frequency we wanted. If one

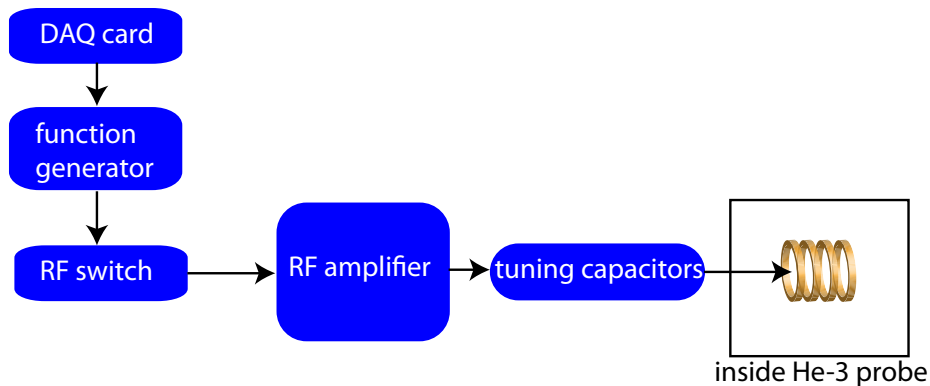


Figure 2.12: Schematic for RF components.

configuration did not work, we resoldered the wires to switch to the other configuration. In our experience, attempting to calculate what the best configuration to use is difficult because there is always something that causes reality to differ greatly from the calculated values.

In order to determine the accuracy of tuning we utilized an HP Network Analyzer. If all the components are very rigid it is possible to tune to within 1% of  $50 \Omega$  and within a few degrees of  $0^\circ$  phase shifts.

Our RF amplifier is an ENI model 5100L-NMR designed to amplify 50 dB with a maximum output of 100 Watts. When performing MRFM experiments, the amplifier must be set to send out continuous waves instead of the pulse waves used in conventional NMR. A RF switch (Mini-Circuits ZFSWHA-1-20) gates the input to the RF amplifier.

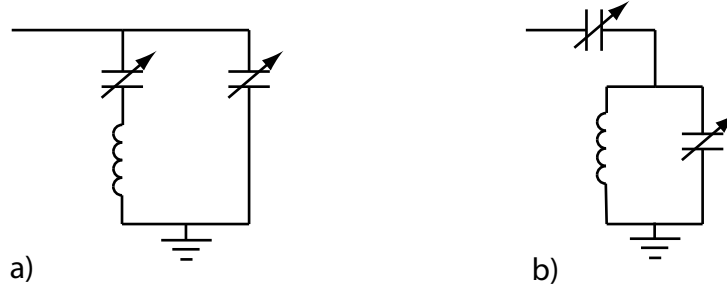


Figure 2.13: a) Parallel matched series tuned b) series matched and parallel tuned.

The RF signal is generated by a Rhode and Schwarz SMH signal generator. For maximum power output we set the output level to 2.0 dBm instead of 0 dBm since there is some loss going through the RF switch. In order to achieve accurate modulation the modulation input should be set to 0.707 V and the modulation frequency controlled through the front panel of the signal generator.

Finally, the modulation signal and gating pulses are generated by a Labview program. Using a DAQ card the modulation waveform is generated through individual points. Due to restrictions in the hardware the smallest pulse we are able to generate is  $1 \mu s$ , which is sufficient for most applications. Our modulation first starts several hundred kilohertz off resonance and then a slow ramp over 10 ms brings the spins into resonance. We set the modulation frequency to be the maximum amplitude allowed by the adiabatic condition since this yields the largest signals,  $\Omega \ll (\gamma B_1)^2 / \omega_{osc}$ , see section 1.7. Our

modulation scheme utilizes a triangular waveform since it generates the clearest artifacts, which will be discussed later in the chapter. In addition to the modulation, our Labiew program also simultaneously sends out a gating pulse to the Nicolet digitizer as well the RF switch. It also sends out a reference frequency for the lock-in amplifier that is matched to the modulation frequency.

## 2.8 Lock-in detection

A lock-in amplifier is essentially a device that only amplifies signals at a specific frequency. However, obtaining good data requires the user to correctly set the time constant. The time constant,  $\tau$ , is defined in terms of the frequency bandwidth of detection,  $\Delta f$ ,

$$\Delta f = \frac{1}{4\tau} \quad (2.7)$$

The higher the time constant the smaller the bandwidth of detection and thus less noise is present. Obviously, we would like to keep the time constant as large as possible to reduce the noise, however, that would only work if all signals are perfect delta functions. Unfortunately, time-varying signals have some spread across a main central frequency and when we perform a scan we must choose the right time constant to accurately ascertain what the cantilever signal is.

Let us examine an example of what happens when the incorrect time constant is used. In Fig. 2.14 we show artifact signals obtained at different time constants. The first thing to note is that for a small time constant the

waveforms are noisy. This should be expected since we are increasing the bandwidth and introducing more noise into the system. The next thing to notice is that for larger time constants the amplitude decreases. Increasing the time constant, or reducing the frequency bandwidth, cuts out important parts of the signal because our field of view is too narrow, thus eliminating contributions to the signal. In addition, the peak of the curves occur later as the time constant is increased. The  $Q$  of the cantilever also plays a role. Small  $Q$  cantilevers will ring down slowly after a CAI pulse and across a large frequency spread. Large  $Q$  cantilevers ring down quickly and over a small frequency spread. The time constant should be chosen so that for small  $Q$ 's a longer time constant is chosen while for large  $Q$ 's a shorter time constant is possible. For larger time constants, it takes a longer amount of time to detect the signal so the peaks occur later. So which peak is the correct one? In this case, the CAI sequence was applied for 95 ms so the maximum cantilever signal should occur at 95 ms. From the figure we can see the peak of the waveform with a time constant at 50 ms is just above 100 ms. If we decrease the time constant to 20 ms, the peak moves towards 50 ms. Thus, in this case we would choose to run the experiment with a time constant of 50 ms since it most closely represents what the true signal is. Finding the right peak requires you to know roughly what it should look like beforehand.

Another example that illuminates how to use the lock-in is a driven scan of the cantilever. In a driven scan we utilize a function generator to send a signal to the shaker piezo next to the cantilever to induce driven oscillations

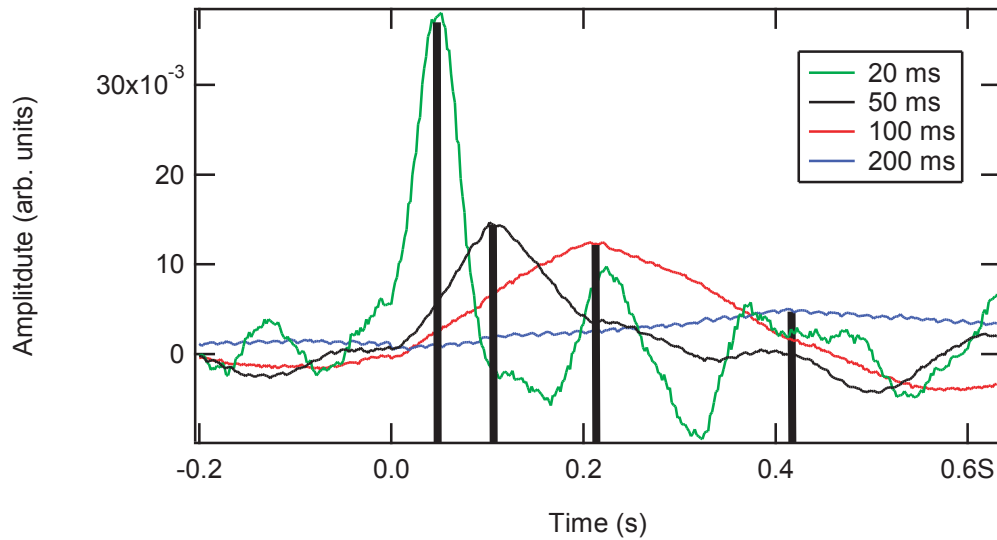


Figure 2.14: Artifacts for 20 ms, 50 ms, 100 ms, and 200 ms time constants with the center of each peak marked by a black line.

of the cantilever at certain frequencies. By sweeping the frequencies across an appropriate range, the resonance peak of the cantilever can be found, as shown in Fig. 2.7. While we are scanning, the function generator is simultaneously sending a signal to the reference input of the lock-in. This signal tells the lock-in at what frequency it should be targeting. Without this reference signal the lock-in will have no idea at what frequency it should look for AC oscillations of the cantilever. The reference signal is multiplied by the actual signal and the result is integrated to yield a DC signal that is sent to an oscilloscope.

## 2.9 Variable temperature insert

For low temperature and variable temperature operation in our NMR magnet we utilize a Janis variable temperature insert (VTI). The VTI consists of four separate chambers: the sample tube, helium reservoir, nitrogen reservoir, and vacuum spaces separating the the three chambers. Before each use we pump out the vacuum space to a high vacuum to prolong the VTI's cryogen hold time. In addition we flush out the needle valve connecting the helium reservoir and sample space with nitrogen or helium gas in order to blow out any blockages. The VTI is capable of achieving a base temperature of 4.2 K and by pumping on the sample space we can attain 1.5 K. Variable temperature control is achieved through adjusting the needle valve and the amount of helium entering the sample space. Our past two Janis VTI's were damaged beyond repair because of a design flaw that made it easy for water to accumulate in the nitrogen reservoir. The newer design makes this water accumulation more difficult, but just to be safe we flush out the nitrogen reservoir with nitrogen gas before each usage.

## 2.10 RF artifact

When we apply CAI pulses the cantilever amplitude will ramp up regardless of whether a spin signal is causing it or not. We term this excitation an artifact and the source of this phenomenon is not well understood. A commonly-believed reason is heat generated by the coil modulated by the CAI, causing eddy currents to oscillate and causing the cantilever to ring up

[27]. However, in contradiction to this explanation often times we will observe an artifact due to an unmodulated RF pulse. Thus, we are not entirely sure of its origins except that heat seems to play some role. Yet, if the artifact level is constant then we can subtract it out as a background. A phase cycling scheme sends out a negative CAI pulse right after a positive one to cancel out the effects of the artifact [28].

Nevertheless instead of being a nuisance of noise it is a convenient way for us to check that our microscope is operating properly. Before starting a NMRFM experiment we check that the artifact level is constant. If the artifact level is not constant it makes it difficult to subtract it out as a background and see the spin signal. A fluctuating artifact usually implies either the cantilever was damaged during sample loading, epoxy has run on over large parts of the cantilever causing nonlinear oscillations, the cantilever is not centered in the coil, or the coil is not connected properly to the rest of the tank circuit.

## 2.11 Gradient magnet

The gradient magnet is one of the key components to obtaining high resolution measurements using MRFM. For our experiments we chose to use Permalloy wire as our gradient magnet. Permalloy generates a modest magnetic field and gradient when placed several hundred microns away from the sample. We determine the saturation magnetization of the magnet with a superconducting quantum interference device (SQUID). Then by using the



following equation

$$B(z) = 2\pi M_0 \left[ \frac{z + L/2}{\sqrt{(z + L/2)^2 + a^2}} - \frac{z - L/2}{\sqrt{(z - L/2)^2 + a^2}} \right] \quad (2.8)$$

we can determine the field profile [29].

Determining the value of the field gradient at various positions is crucial for obtaining accurate images. However, values determined from geometry calculations are only approximate since they assume the magnet is perfectly spherical, circular or otherwise ideal. One method to measure the gradient field *in situ* is to measure the force at various magnet-sample separations while varying the magnetic field. The derivative of the resulting curve will yield the field gradient. However, this method suffers in that if distances are not calibrated accurately in your probe the results will only be approximate, albeit with higher precision than estimates from geometry. Recently Choi et al. have proposed a high resolution *in situ* gradient magnet calibration that does not require calibration of distance between the sample and magnet [30]. An ultrasensitive cantilever resembling the types used in NMRFM is fabricated with a small superconducting annulus at its end, see Fig. 2.15. The cantilever has a spring constant around  $10^{-4}$  N/m and  $Q$  greater than 1000 while the annulus is composed of niobium with a diameter of approximately  $20 \mu\text{m}$  and a  $T_c$  of 9 K. When the annulus is superconducting, magnetic flux through the annulus is quantized in units of the flux quantum  $\Phi_0 = h/2e = 2.07 \times 10^{-15}$  Wb. Thus the magnetic moment in the annulus increases stepwise depending on the number  $n$  of trapped flux quanta. The interaction between

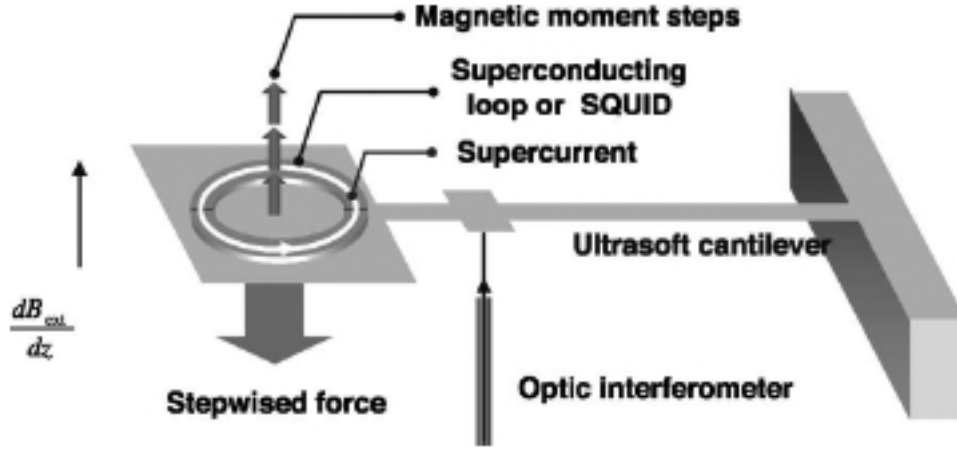


Figure 2.15: Schematic of ultrasensitive cantilever with superconducting annulus

the magnetic moment and an external gradient field produce a stepwise force on the cantilever

$$F = m \frac{dB}{dz} \quad (2.9)$$

where  $m$  is the magnetic moment and  $\frac{dB}{dz}$  the field gradient, this is very similar to NMRFM detection. Thus one possible setup to measure the field gradient is to use a cylindrical magnet with its face parallel to the annulus and move it in 3-D with respect to the annulus and through measuring the response determine the magnitude of the field gradient at various positions of the gradient magnet.

In order to resolve what the field gradient is we first note that the magnetic moment felt in the ring can be written as

$$m(n, B_{ext}) = m_1(n) + m_2(B_{ext}) \quad (2.10)$$

where  $m_1(n)$  is the quantized flux and  $m_2(B_{ext}) = \chi B_{ext}$  from the magnet, where  $\chi$  is the magnet susceptibility. Then using Eq. 2.10 we can write the force in the  $z$ -direction as

$$F(z) = (m_1(n) + m_2(B_{ext})) \frac{dB}{dz}. \quad (2.11)$$

If we expand  $B$  about equilibrium position  $B_0$  then Eq. 2.11 becomes

$$F(z) = (m_1(1)n + \chi B_0) \frac{dB}{dz} + \chi \left( \frac{dB}{dz} \right)^2 z. \quad (2.12)$$

Then relating the change in resonance frequency to a change in the spring constant

$$\frac{\Delta\omega}{\omega} = \frac{1}{2} \frac{\Delta k}{k} \quad (2.13)$$

we obtain

$$\frac{\Delta\omega}{\omega} = \frac{\chi}{2k} \left( \frac{dB^2}{dz} \right) \quad (2.14)$$

[31]. This yields the field gradient as a function of the shift in resonance frequency. However, if we want to be more precise by measuring at the level of individual flux quanta then we set the displacement of the cantilever  $\Delta z = z_{eq}(n) - z_{eq}(n = 0)$  and note that at  $z = \Delta z$ ,  $F(\Delta z)$  is at equilibrium with  $(k + \Delta k)z_{eq}$  thus yielding can

$$\frac{dB}{dz} = \frac{2n}{\Delta z} \frac{m_1(1)}{\chi} \frac{\Delta\omega}{\omega}. \quad (2.15)$$

Every newly introduced flux quanta  $n$  results in a slight change in the field gradient. This is important when calibrating for very small distances. If we assume that  $dB/dz = 10$  T/m,  $k = 10^{-4}$  N/m, and  $\omega = 2$  kHz, then the

resulting change in frequency will be 4 Hz which is well within the limits of most electronics.

We performed a demonstration experiment to determine whether we could resolve the gradient field of a magnet using this setup. A gradient magnet is brought within 1 mm of the cantilever and is scanned towards the cantilever. The cantilever was driven at its resonance frequency and we looked for shifts in frequency from resonance. The resonance frequency was 1504 Hz,  $Q = 1462$ , and  $k = 10^{-4}$  N/m at a temperature of 4 K and pressure of  $10^{-5}$  torr. The resulting data is shown in Fig. 2.16. The frequency steadily decreases as we approach the cantilever implying the loop is admitting larger number of flux quanta,  $n$ , and thus leading to a larger field gradient. However, we do not observe individual flux quanta primarily because at the time we had a difficult time calibrating our nanopositioner for submicron scale steps. In conclusion, a small superconducting loop can be extremely sensitive to changes in magnetic field and magnetic field gradient and with further optimization of our measurement apparatus we should be able to reach the ultimate resolution of individual flux jumps.

## 2.12 Achieving resonance

Detection of a spin signal in MRFM involves varying the magnetic field the sample experiences until the resonance condition is satisfied. There are three methods to vary the field the sample experiences. The first method is to vary the field of the large superconducting magnet. This has the advantage

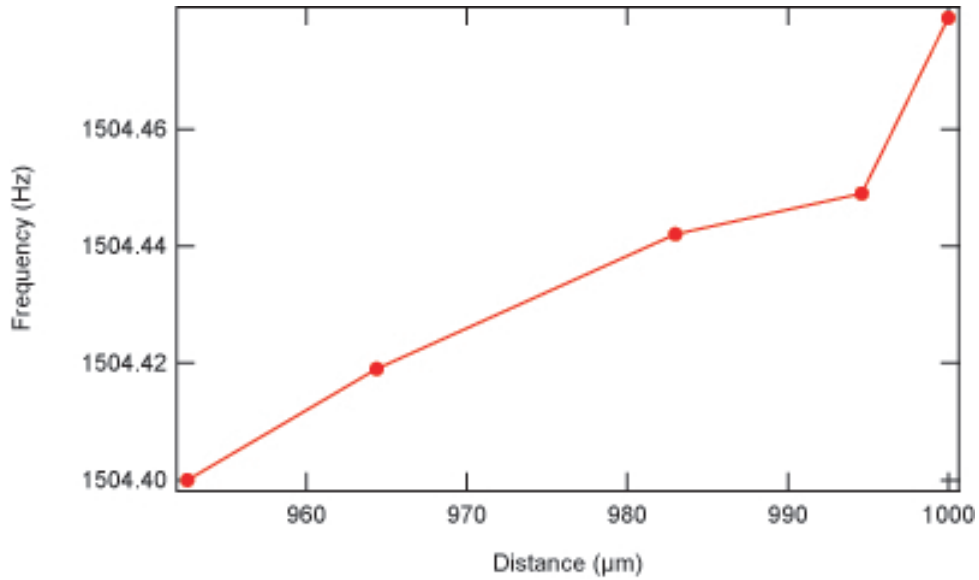


Figure 2.16: Data for z-scan sweep.

in that it is easy to implement for certain magnets, keeps the gradient field constant, and induces no vibrations in the probe due to any moving parts. The drawback is that it consumes helium very quickly at high fields and adjusting the field in NMR magnets like our Cryomagnetics magnet is time-consuming to do. The second method is to physically move the gradient magnet towards and away from the sample. This is the usual method we utilize when operating in the Cryomagnetics magnet to change the field. However, this method has a couple of major drawbacks. First, it changes the gradient field as you move closer to the sample, which must be taken into account when performing image reconstruction. The other drawback is that you have to calibrate the gradient magnet Attocube so it moves steadily at all temperatures. The final disadvantage is that since laser light from the fiber can reflect off the magnet

(due to some transmission through the cantilever), each time you move the magnet you change the photodiode signal, often changing the fringe height. Thus we have to constantly check the fringe height after moving the magnet which can be somewhat time consuming.

The final detection method instead of changing  $H_0$  changes the frequency of  $H_1$  by sweeping the signal generator. Like the first method it requires no moving parts and as a bonus requires no helium boil off. The disadvantage depends on the Q of the tank circuit. If the Q is high then changing the frequency will greatly affect the tuning and possibly prevent you from achieving sufficient  $H_1$  to tip the spins. On the other hand, if the Q is very low, then we can sweep across several MHz without greatly affecting the tuning. One other thing that must be kept in mind is that at different frequencies the artifact level will change. At resonance we realize the lowest artifact level and as we move away from resonance in either direction the artifact level steadily goes up. The reason for this behavior is not apparent to us since it would make more sense for the artifact to have its highest level at resonance since the most power is being applied.

## Chapter 3

### Initial room temperature experiment on ammonium sulfate

#### 3.1 Conventional NMR

One of the most important requirements for obtaining an NMRFM signal is sufficient  $H_1$  strength to overcome the local fields between the nuclei and manipulate the spins. However, in NMRFM we do not know what the  $H_1$  field strength is until we successfully obtain a spin signal and perform a nutation experiment. Thus, we perform conventional NMR experiments using the coil in the NMRFM probe to more directly ascertain what the generated field strength is. We utilize a liquid sample with an abundance of the nuclei of interest and perform FID and spin echo experiments to determine the field strength.

For our conventional NMR experiment our block diagram is illustrated in Fig. 3.1. Details of this type of experiment can be found in Dradnova and Cobb's theses so I will only review the basics of the block diagram [32] [33]. The signal from the transmitter travels to the tank circuit of our probe. A crossed diode box before the tank circuit ensures none of the signal reflects back toward the power amplifier. Our tuning capacitors were located at the

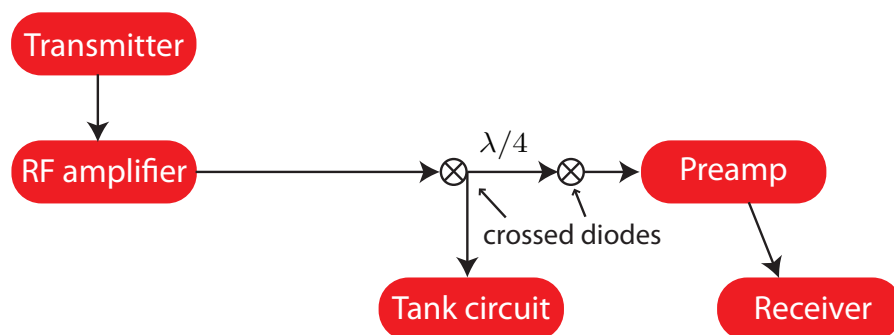


Figure 3.1: Block diagram of conventional NMR experiment

top of the probe away from coil since this enabled us to tune easily while sacrificing some signal. The signal from the tank circuit then travels to a  $\lambda/4$  cable and multiple cross diode boxes to damp out the signal so it does not damage the preamp. The preamp then takes the signal, amplifies it by 28 dBm and sends it towards the receiver.

For our sample we chose  $\text{K}_3\text{PO}_4$  in distilled water because it is  $> 120\%$  soluble in water yielding a relatively high phosphorous concentration. While the NMRFM experiment will be done on protons, we had to choose phosphorous as the nuclei for our conventional NMR experiment because our conventional NMR spectrometer utilizes an 8 T field, while the NMRFM experiment was done in a 3 T field. In addition  $\text{K}_3\text{PO}_4$  is not acidic, so any leaks in our capsule would not adversely affect our probe and magnet. We ran the experiment at 138.9816 Mhz with the sample in the coil of the probe. The resulting



spin echo from a  $\pi/2$ - $\tau$ - $\pi$  sequence is shown in Fig. 3.2 with  $\tau = 5$  ms. We maximized the amplitude of the spin echo by adjusting the length of the  $\pi/2$  and  $\pi$  pulses. Once we determined the length of our  $\pi/2$  pulse we utilized the relation

$$\theta = \gamma H_1 t \tag{3.1}$$

where  $\theta$  is the angle through which the pulse tips the spins and  $t$  is the time of the pulse, to determine the strength of the  $H_1$  field. We find that our  $H_1$  field is 58 gauss which should be more than enough for a solid state experiment. However since we rarely place the sample directly into the coil we need to know the field drop off outside the coil. This is shown in Fig. 3.3 using Eq. 2.7. The field drop off is rather gradual and even at 400 microns from the base of the coil we can realize a field of approximately 42 gauss. Thus our conventional NMR experiment confirmed that we had sufficient  $H_1$  field strength to manipulate the spins for NMRFM.

### 3.2 Experimental Details of Room Temperature Scan

After we had confirmed we had sufficient  $H_1$  field strength to overcome the local fields we proceeded with a NMRFM scan of ammonium sulfate,  $(\text{NH}_4)_2\text{SO}_4$ . We chose ammonium sulfate as our test sample since it has a high density of protons (8 per molecule) providing a very strong signal that can be easily seen. We chose a flake with approximate dimensions of 100  $\mu\text{m}$  by 200  $\mu\text{m}$  by 60  $\mu\text{m}$  as seen in Fig. 3.4. The platelet-like geometry is important because it most closely matches the shape of the resonance slice. By matching

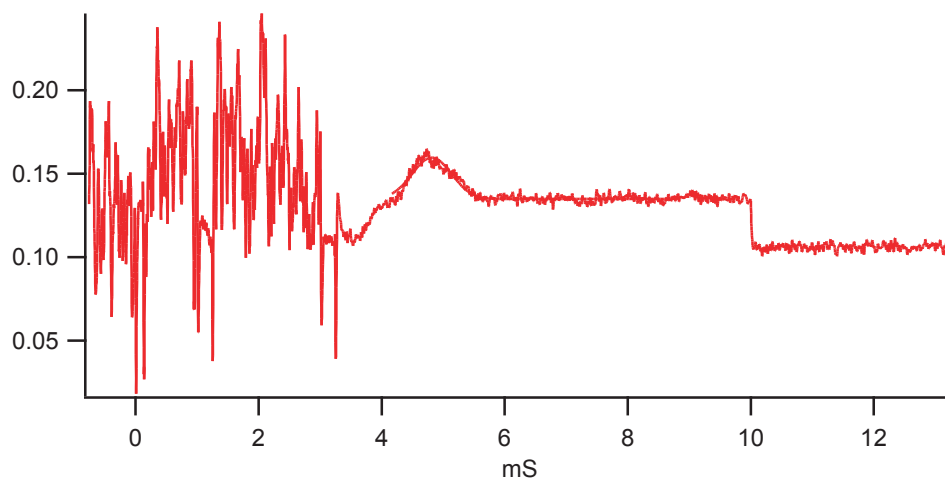


Figure 3.2: Spin echo centered at 5 ms.

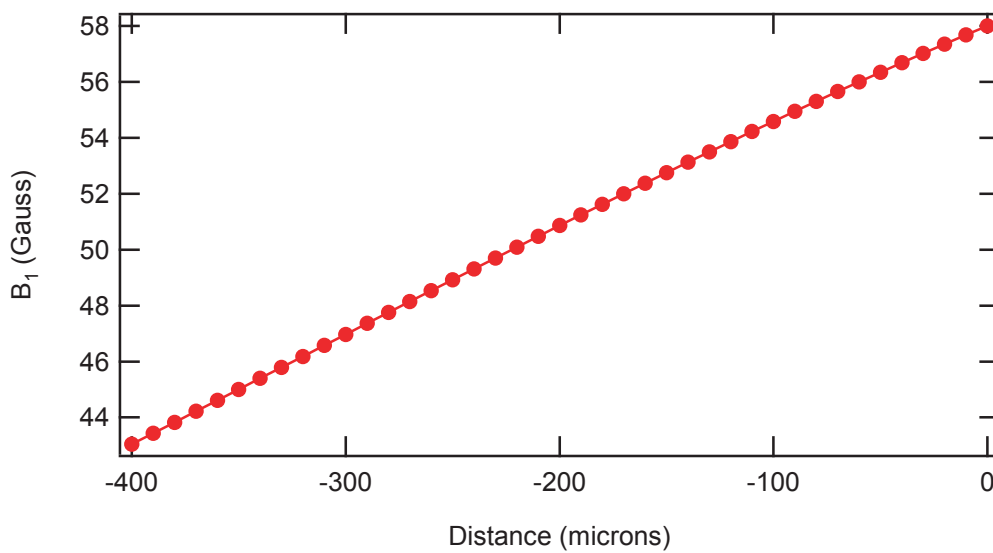


Figure 3.3:  $H_1$  field strength as a function of distance away from the bottom of the coil.

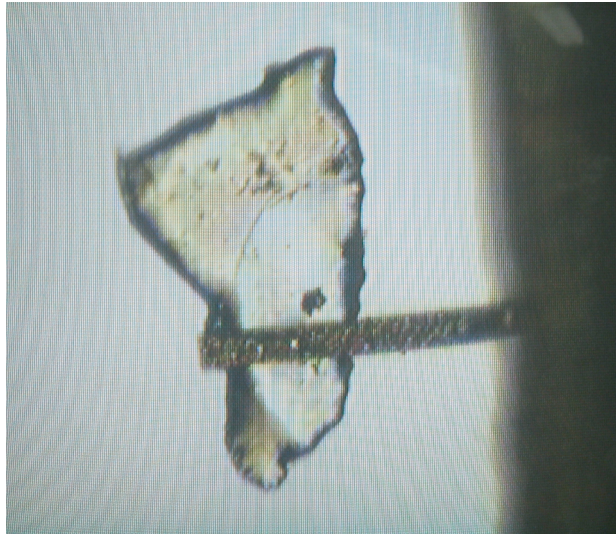


Figure 3.4: Picture of the sample on the cantilever.

the sample geometry to the shape of the resonance slice we can maximize the number of spins detected within the resonance slice, yielding a large signal. The sample was first prepared by taking large single-crystal pellets of ammonium sulfate, crushing them into smaller grains and then mounting them onto the cantilever with silver epoxy.

The cantilevers we used were Veeco tipless AFM cantilevers with a spring constant of 0.03 N/m. Although its force sensitivity is nearly 20 times smaller than that of the long, thin high sensitivity cantilevers, we chose to use the Veeco cantilevers since they were cheap and easy to find with the fiber interferometer due to their large size. After mounting the sample on the cantilevers the resonance frequency was 1.488 kHz with a quality factor of 500.

For our gradient magnet we utilized a commercial Permalloy wire (MWS

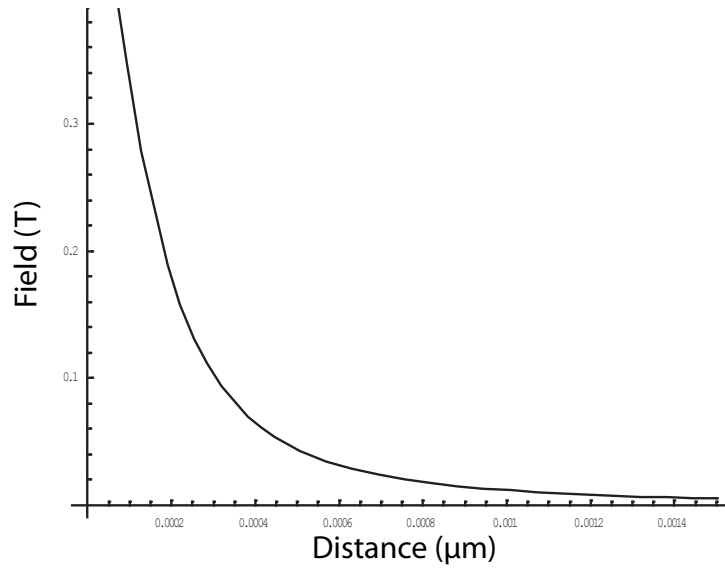


Figure 3.5: Permalloy magnet field strength as function of distance away from the sample.

Alloy 120) with a diameter of 0.40 mm. Since we wanted to maximize the signal and not perform high resolution scans in this experiment we chose this magnet size to realize a large resonance slice. In addition, the larger size made aligning with the cantilever much easier. SQUID measurements performed on a small Permalloy sample yielded a magnetization of  $9.39 \times 10^5$  emu/cm<sup>3</sup>. From this we calculated the gradient and magnetic field curves as shown in Figs. 3.5 and 3.6. We chose to place the magnet 307  $\mu\text{m}$  away from the sample to yield  $B_{magnet} = 0.1$  T and  $\nabla B = 500$  T/m. These parameters are on a more linear region of the gradient and magnetic field curves, so that changes in position would not result in nonlinear changes in both the gradient and magnetic field.

In order to determine the amplitude of our cyclic adiabatic inversion

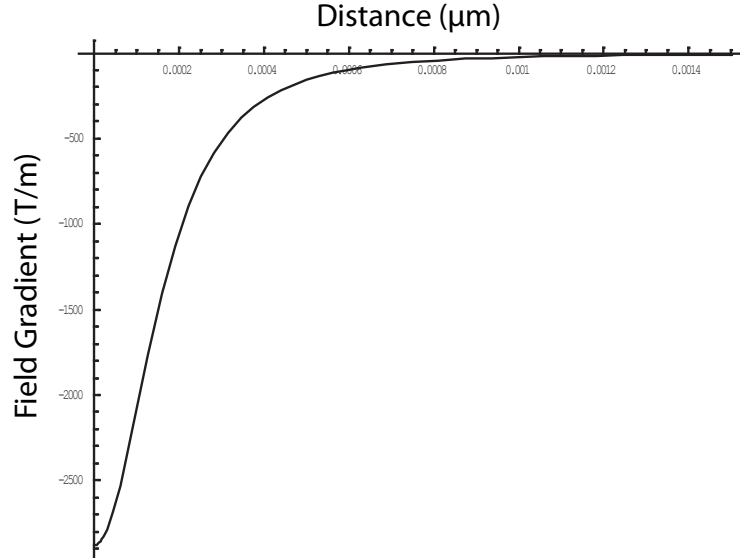


Figure 3.6: Permalloy magnet gradient field magnitude as function of distance away from the sample.

we utilized Eq. 1.36 with  $\gamma_{protons} = 42.58 \text{ MHz/T}$  and assumed  $H_1 = 10 \text{ gauss}$  (as a conservative estimate). We thus obtained

$$\frac{((42.58 \times 10^6 \text{ MHz/T})(10^{-3} \text{ T}))^2}{1488 \text{ Hz}} = 1.22 \text{ MHz.} \quad (3.2)$$

The adiabatic condition is satisfied as long as we are 6 times smaller than this. In our case, we wished to remain conservative and chose a lower  $\Omega$  to ensure we got as large a signal as possible; thus we chose a value 10 times smaller at 125 kHz. This was high enough so we could realize a stable artifact signal.

Then using Eq. 1.37 we find that the resonance slice width is

$$\Delta z = \frac{2\Omega}{\gamma \nabla B} = 11.7 \text{ } \mu\text{m.} \quad (3.3)$$

This resonance slice width is smaller than our sample thickness ( $60 \mu\text{m}$ ) enabling us to perform 1-D imaging scans. If we were to choose a resonance slice with a thickness equal to the sample this would have given us the largest possible signal, but with loss of spatial resolution.

The minimum detectable force using Eq. 1.34 for room temperature and a time constant of 50 ms is

$$F_{min} = \sqrt{\frac{4(0.03 \text{ N/m})k_B T(1/(4(.05 \text{ s})))}{2\pi(1488 \text{ Hz})(500)}} = 1.45 \times 10^{-14} \text{ N} \quad (3.4)$$

In order to calculate the force produced we first determine the number of available protons. We are going to assume that our sample resembles a rectangular block so the area is

$$100 \mu\text{m} \times 200 \mu\text{m} = 20000 \mu\text{m}^2 = 2 \times 10^{-4} \text{cm}^2. \quad (3.5)$$

The thickness is determined by the resonance slice, which is  $11.7 \mu\text{m}$ . Thus our volume is

$$(2 \times 10^{-4} \text{cm}^2)(11.7 \mu\text{m}) = 2.34 \times 10^{-7} \text{cm}^3. \quad (3.6)$$

The density of ammonium sulfate is  $1.77 \text{ g/cm}^3$  so the mass of our sample in the resonance slice is

$$(1.77 \text{ g/cm}^3)(2.34 \times 10^{-7} \text{cm}^3) = 4.14 \times 10^{-7} \text{g}. \quad (3.7)$$

To find the number of atoms we use Avogadro's number and the molar weight of ammonium sulfate

$$(4.14 \times 10^{-7})\left(\frac{1 \text{ mole}}{132 \text{ g/mole}}\right) = 3.14 \times 10^{-9} \text{ moles} \quad (3.8)$$

$$(3.14 \times 10^{-9} \text{ moles})(6.022 \times 10^{23} \text{ molecules/mole}) = 1.89 \times 10^{15} \text{ molecules.} \quad (3.9)$$

And since there are 8 proton per molecule we finally obtain

$$8(1.89 \times 10^{15}) = 1.51 \times 10^{16} \text{ protons.} \quad (3.10)$$

Inserting this into Curie's Law we obtain

$$\frac{(1.51 \times 10^{16})(2\pi\gamma\hbar)^2(8.1)(500)}{4k_B T} = 2.96 \times 10^{-12} \text{ N.} \quad (3.11)$$

Thus the SNR is 204. However, as we will see the actual SNR is much smaller due to the resonance slice shape.

We utilized a triangular modulation centered at 138.9931 MHz and at 2 dBm produced by our Rhode and Schwarz SML 01 signal generator. The signal was then sent to the RF switch and then to the ENI 5100L power amplifier which amplified it 48 dBm to a 50 dBm signal to the tank circuit. Naturally there are some losses including those from the RF switch and poor tuning, so our final power at the coil was probably much less than 50 dBm, which corresponds to 100 W of power.

In order to calibrate the gradient magnet stage movements we utilized the fiber interferometer and counted fringes as described in section 2.4 as we had not conceived of resistor or capacitive detection yet. Under real experimental conditions we noticed that the stages seemed to move very little compared to what we had calibrated or not all. We had always calibrated by moving several fringes up and down a certain point, however that proved to

be inaccurate because that calibration only applied for a couple of microns and only at that specific point on the graphite rod. Thus we utilized a cruder method of calibration with less precision but much better accuracy. We first used a digital camera, with a microscope as the zoom lens, to take a picture of the gradient magnet with respect to the cantilever. Since we already know what the gradient magnet diameter is when we view the picture on the computer we can measure what the magnet to cantilever distance is, albeit with only  $10\ \mu\text{m}$  resolution. We then pulse single sawtooth waves and move the gradient magnet several hundred microns since that corresponds to the amount of movement that we utilize in a typical experiment. We then take another picture and measure the new magnet to cantilever spacing. The difference between the spacing divided by the number of pulses determines the distance traversed per pulse. Obviously this is much cruder than fiber detection since we are using a digital camera to measure distance and we have only plotted two points and have neglected hysteresis in the stages, but we were able to attain a fairly accurate measurement of the distance our magnet stage traversed for a given number of pulses.

The NMRFM experiment was then performed by scanning the z-stage at  $10\ \mu\text{m}$  intervals to search for the resonance condition. A stable artifact signal enabled us to subtract it off as a baseline noise source. We signal averaged 4-9 times, but once a stable signal was found we took single-shot measurements. The results of our scan are shown in Fig. 3.7 along with another scan with a shift in resonance frequency to confirm the origin of the NMR signal. Our



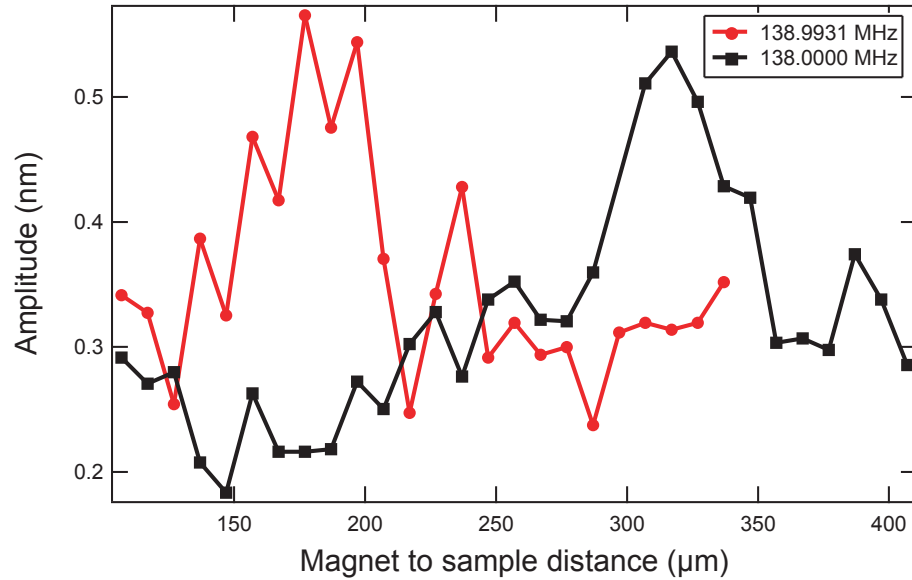


Figure 3.7: 1-D scan results with accompanying frequency shift. The 150  $\mu\text{m}$  shift is consistent with that expected for the calculated magnetic field distribution due to the field gradient magnet (see text).

observed shift was 150  $\mu\text{m}$  which agrees well with the expected shift of 145  $\mu\text{m}$ . The widths of the peak correspond to a sample with approximately 25  $\mu\text{m}$  thickness. This is different from the actual thickness we measured through a microscope, but we have to take into account the presence of the resonance slice.

The oscillator maximum amplitude was 1.66 nm yielding a force of  $10^{-13}$  N which corresponds to a SNR of approximately 6.9, roughly 30x smaller than expected. The primary reason our actual SNR differs so greatly from the predicted SNR is that the resonance slice only penetrates a small portion of the sample, see Fig. 3.8. We attribute most of this to misalignment between the

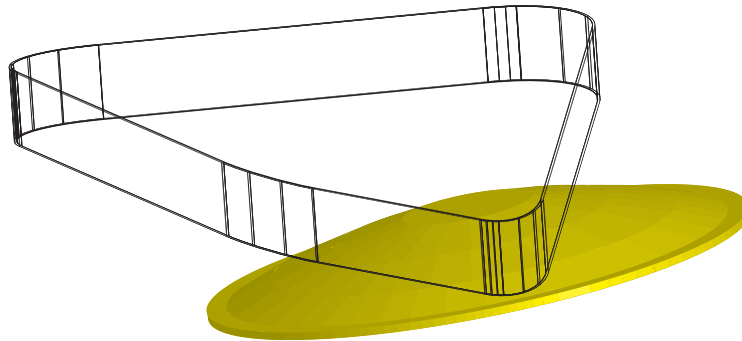


Figure 3.8: Our resonance slice, in yellow, was only intersects a small portion of the sample due to misalignment between the gradient magnet and sample.

gradient magnet and sample. This displaces the resonance slice with respect to the center of the sample

We then performed a nutation experiment to demonstrate coherent control of the spins as well as ascertain the strength of the field from our RF coil. In a nutation experiment you tip the spins at various angles and then observe the resulting signal to see how many of the spins had followed the tipping pulse. Due to relaxation effects, the longer the pulse, more and more spins will decohere. In addition the length of the pulse is related to  $H_1$  through Eq. 3.1. Determining the length of a  $\pi/2$  pulse will tell us our  $H_1$  field strength. The pulse sequence we utilized is a  $t_{pulse} - \tau - CAI$  sequence and varying the length of  $t_{pulse}$ . The data is shown in Fig. 3.9 and there is a

distinct nutation signal with a period of 20  $\mu\text{s}$ . We fit the data to the function

$$f(t) = e^{-t_{pulse}/u} \cos(\gamma H_1 t_{pulse}) + C \quad (3.12)$$

and find that  $H_1$  is approximately 13.6 G. The fact that we see 3-4 distinct wavelengths shows that we are able to coherently control the spins using RF pulses. In addition, the strong nutation signal allows us to perform pulse sequences with varying times and not worry about losing too many spins. Lastly, the magnitude of our  $H_1$  field shows that we have more than enough field strength to overcome the local fields (typically around 3 G) between the closely-spaced hydrogen nuclei to manipulate the proton spins. However, the field strength is much smaller than anticipated from our conventional NMR experiment and we postulate that this might be due to the coil not being an exact solenoid shape contributing to a larger field drop off outside of it or the sample was not centered directly along the central axis of the coil where the field drop off is steep.

We next executed a spin echo measurement to demonstrate relaxation measurements. We utilized a  $\pi/2$ - $\tau$ - $\pi$ - $t$ - $\pi/2$ -CAI pulse sequence. From the nutation experiment we found the length of our  $\pi/2$  pulse to be 5  $\mu\text{s}$  and  $\pi$  pulse to be 10  $\mu\text{s}$ . Unlike conventional NMR we cannot continually observe the evolution of the spins across time, instead we take snapshots of the spins at specific points in time. Thus, to map out the spin echo we set  $\tau = 17 \mu\text{s}$  and then vary the time  $t$  before the sampling  $\pi/2$  pulse to map out the echo [34]. Fig. 3.10 shows the result of our measurement with the peak of the

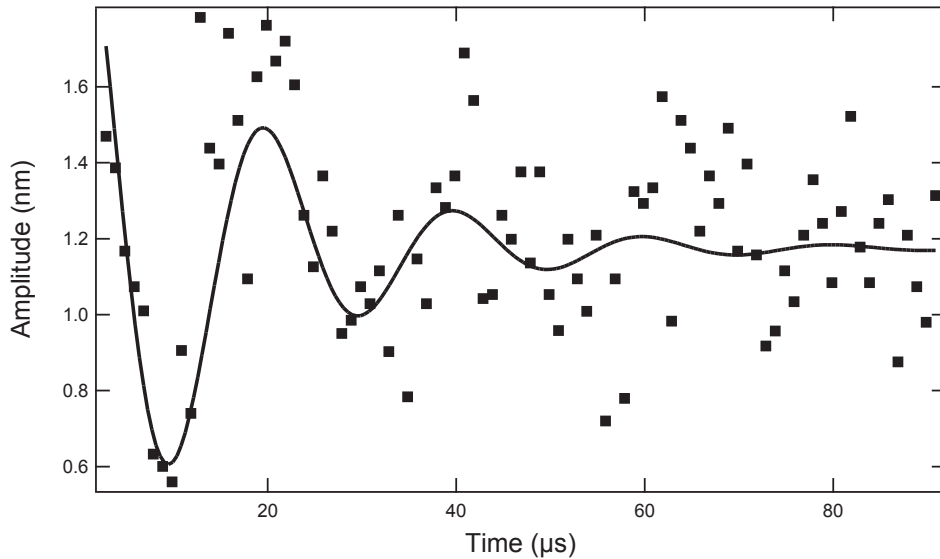


Figure 3.9: Spin nutation signal shown across multiple periods.  $H_1$  is calculated using  $\pi/2 = \gamma H_1 t$  where  $\gamma$  is the gyromagnetic ratio and  $t$  is the length of the pulse.

spin echo occurring near  $17 \mu s$  as it should. The full width at half maximum was measured to be  $8 \mu s$  where most of the shape of the signal is due to the inhomogeneity of the gradient field and not the spin-spin interaction as is common in conventional NMR. The ringing after pulses makes it extremely difficult to observe such a short timescale spin echo signal using conventional NMR.

Finally we attempted a spin lattice relaxation measurement. We utilized a saturation comb consisting of 5  $\pi/2$  pulses separated by  $200 \mu s$  each. We then waited a time  $t$  before applying our CAI pulse to observe how many of the spins had relaxed back to their equilibrium position. Our results are shown in Fig. 3.11. Since we utilized an inversion sequence we would like to

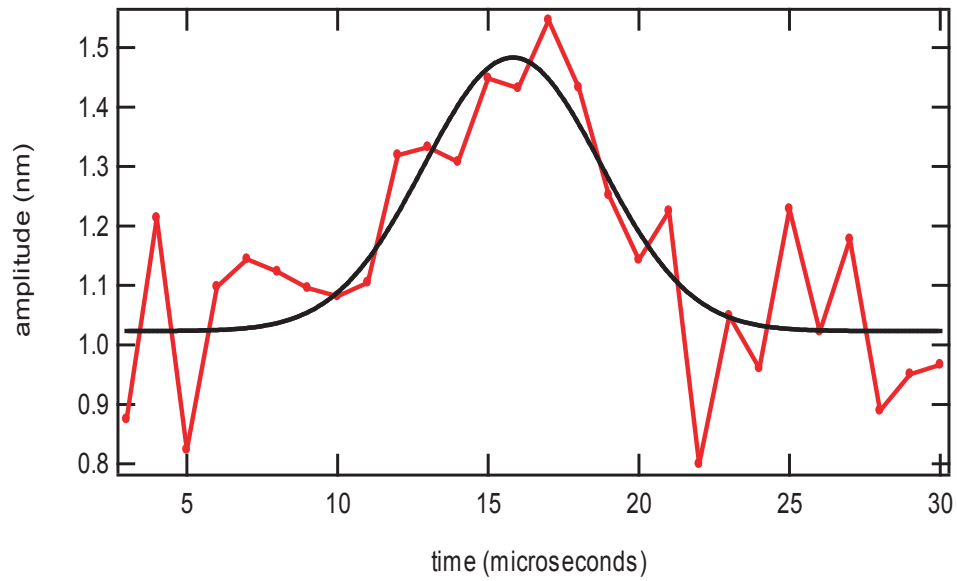


Figure 3.10: Spin echo centered near  $17 \mu\text{s}$ .

fit to

$$M = M_0(1 - 2e^{-t/T_1}) \quad (3.13)$$

however, due to limitations in our experimental setup at the time we could not take data beyond 1400 ms and so the curve never saturates as it should. Thus, fits to the data using Eq. 3.13 are poor and we are unable to determine what the spin-lattice relaxation time is.

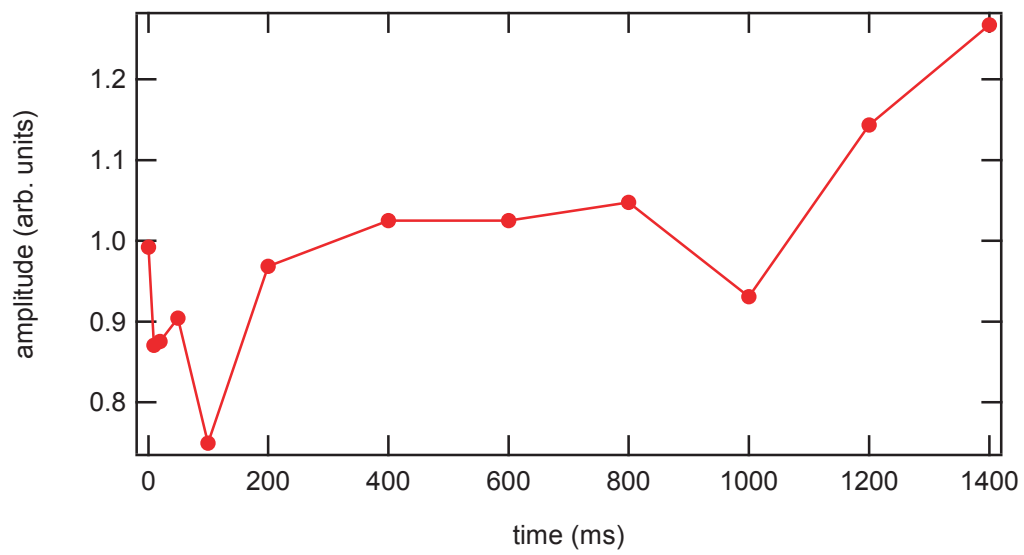


Figure 3.11: Results from inversion recovery sequence

## Chapter 4

# NMRFM studies of Magnesium Diboride

### 4.1 Magnesium diboride background

The discovery of magnesium diboride ( $\text{MgB}_2$ ) took the physics world by surprise in 2001 because it possessed the highest transition temperature,  $T_c = 39$  K, of any intermetallic compound, well higher than what had been predicted from the BCS framework [35]. Immediately, groups set out to determine the order parameter for the Cooper pairs in order to help ascertain the origin of its relatively high  $T_c$ . NMR is a good method for determining the superconducting parameters ever since Hebel and Slichter verified the validity of BCS theory by seeing a coherence peak in spin lattice relaxation measurements [36].

$T_1$  relaxation is due partially to conduction electrons in an initial state scattering to a final state resulting in a change in both the momentum and spin; the nuclear spins simultaneously change energy levels to conserve angular momentum. In metals, the temperature dependence of  $T_1$  can be well approximated by the Korringa product

$$\frac{1}{T_1 T K_s^2} = \frac{4\pi k_B \gamma_n^2}{\hbar \gamma_e^2} \quad (4.1)$$

where  $K_s$  is the Knight shift and  $\gamma_n^2$  and  $\gamma_e^2$  are the nuclear and electron gyromagnetic ratios, respectively [37]. In the superconducting state  $T_1$  changes

dramatically since a portion of the fermions are paired into singlet states and do not scatter. The condensing of electrons into a coherent ground state also causes a coherence factor to arise when calculating  $T_1$  [38] [39]. Just below  $T_c$  this causes  $1/T_1$  in the superconducting state to greatly exceed  $1/T_1$  in the normal state resulting in a coherence peak. Then as the temperature is gradually lowered,  $1/T_1$  decays exponentially. We note that BCS s-wave superconductors are known to possess coherence peaks, but superconductors with unconventional pairing, such as the cuprates, produce no coherence peak.

The first NMR studies carried out on  $\text{MgB}_2$  were done on polycrystalline samples. Fabrication of single crystals large enough for conventional NMR had not been accomplished yet so the only way to achieve an acceptable filling factor in the coil to realize a large enough signal was to use polycrystals. This makes the NMR results difficult to interpret since polycrystals have a large range of crystal orientations, thus mixing contributions from different directions and possibly washing out a coherence peak. The first set of NMR spin lattice relaxation measurements reflect this uncertainty, see Figs. 4.1 and 4.2. Kotegawa et al.'s spin lattice relaxation data show no clear coherence peak [40]. They claim that by plotting  $(1/T_{1s})/(1/T_{1n})$  they observe a small peak just below  $T_c$  which infers that  $\text{MgB}_2$  is a strong coupling s-wave superconductor. However, from BCS theory this increase should have been much greater.

Later NMR studies by Canfield et al. show no coherence peak either; they conclude the use of polycrystals prevents them from obtaining a reliable



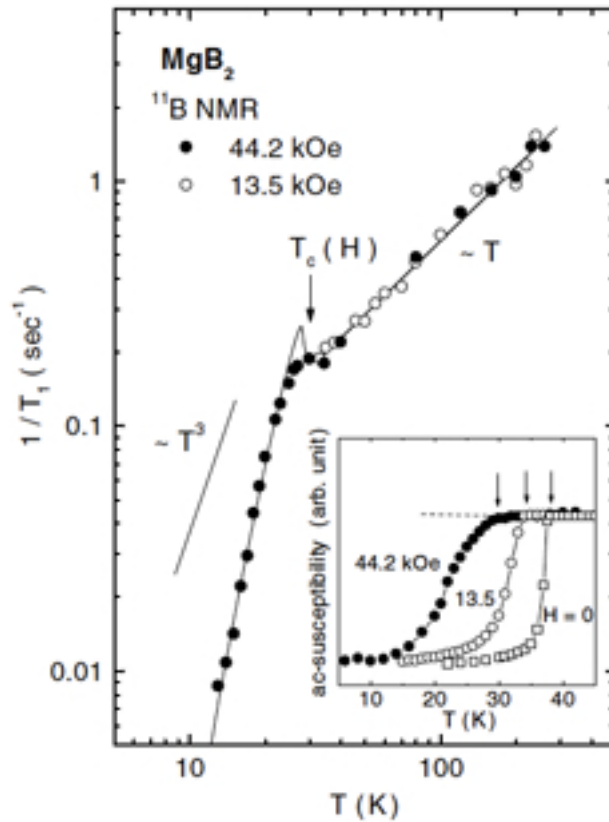


Figure 4.1: Spin Lattice relaxation measurements of polycrystalline  $MgB_2$  at two different fields. Inset: ac susceptibility measurements at various fields [6]

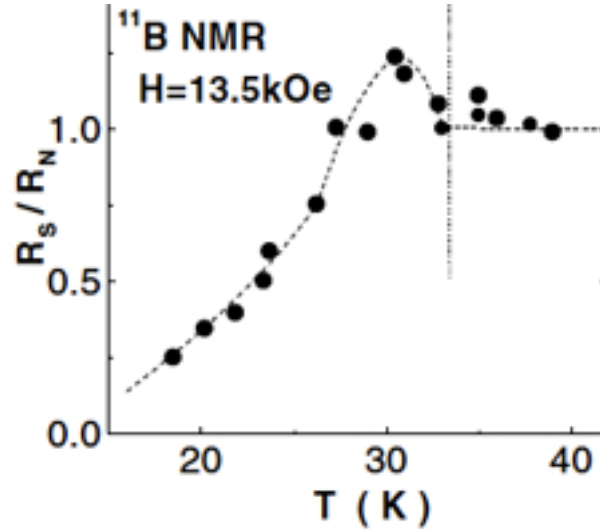


Figure 4.2:  $R_s/R_n = (1/T_{1s})/(1/T_{1n})$  v. temperature. A small peak is observed just below  $T_c$  [6]

interpretation of their data [41] [42]. It was at this point that Jae-Hyuk Choi, a former postdoc in our lab, proposed using NMRFM to probe the spin lattice relaxation of  $\text{MgB}_2$ . At the time, the largest single crystals were roughly  $20 \mu\text{m}$ , much too small for conventional NMR, but more than large enough for NMRFM. However, before any results could be obtained in our lab new fabrication methods for large single crystals, approximately 1 mm, were developed [43] [44]. Thus it seemed any inherent advantage NMRFM had over conventional NMR was negated. Spin lattice relaxation measurements on these single crystals yielded a Korringa like linear behavior above  $T_c$ . However, below  $T_c$  it was found that the diamagnetic shielding caused a large drop in SNR, such that probing the spin lattice relaxation time below  $T_c$  was not possible. NMRFM with its far superior sensitivity should be able to navigate around this

problem and thus an opportunity exists for NMRFM to make an impact on the elucidation of the pairing symmetry of MgB<sub>2</sub>.

## 4.2 NMRFM experimental considerations

One of the primary difficulties facing NMR detection of the boron resonance in MgB<sub>2</sub> is that boron's nucleus is a quadrupole with spin 3/2, instead of 1/2 as in nuclei like protons. Referring back to Fig. 1.1 instead of just one possible transition between  $I = -1/2$  and  $I = 1/2$  we now have three possible transitions as shown in Fig. 4.3 [45]. In a strong magnetic field the energy levels are shifted slightly from  $E_m = -\gamma\hbar H_0 m$  resulting in different  $\Delta E$ 's between the energy levels and thus corresponding to three different resonance frequencies. The -1/2 to 1/2 transition (or vice versa) is unshifted, in first order, from the spin 1/2 case. The other two cases are shifted and thus produce resonances above and below the -1/2 to 1/2 transition. The -1/2 to 1/2 transition remains the most probable transition and the relative intensities of the three transitions are 3:4:3 [46] Thus, the boron -1/2 to 1/2 transition is only 40% as intense as compared to the same transition in a spin 1/2 nuclei.

In addition, the quadrupole broadens the linewidth of each of the three transitions. If we think of a resonance curve with a small frequency linewidth then broadening the line means expanding to a curve with a large frequency linewidth while maintaining the same area under the curve since the net magnetic contributions remain the same. Thus, for broad linewidths, there is a loss in signal at every frequency in the line. On top of the quadrupole broadening

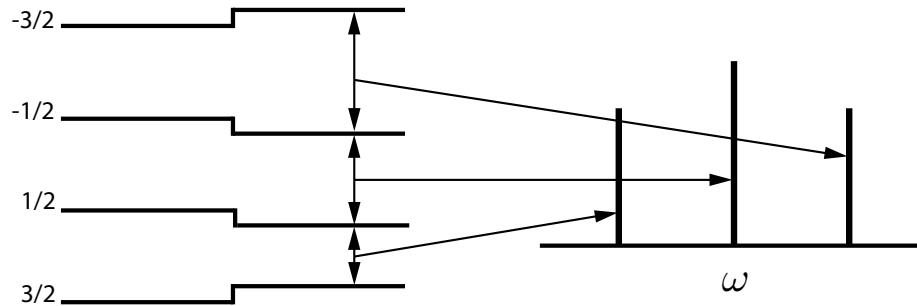


Figure 4.3: Left: quadrupole energy levels and shifts. Right: corresponding resonance lines and arrows showing which transition corresponds to which line.

there is also broadening from the gradient magnet. This is one of the main drawbacks of MRFM in that higher spatial resolution comes at a slight cost of signal strength.

For our initial experiments we chose to examine a powder sample of  $\text{MgB}_2$  at 77 K. Single crystals are difficult to come by so we wanted to conserve their use until we were sure we could see a boron resonance signal using NMRFM. However, the drawback of using a powder is random alignment of the grains causes line broadening. Thus, in total, we are faced with at least four factors which make observing the boron resonance much more difficult than typical spin  $1/2$  nuclei.

### 4.3 Preliminary NMRFM data on MgB<sub>2</sub>

We prepared our samples by taking MgB<sub>2</sub> powder (Aldrich) and making a 90/10 mixture of powder and 5-minute epoxy to obtain clumped powders that were on the order of 30  $\mu\text{m}$  on each side. We utilized a smaller coil with approximate dimension of 800  $\mu\text{m}$  in diameter to generate larger  $B_1$  fields. For our experiment we chose a sample with approximate dimensions of 30 x 30 x 30  $\mu\text{m}^3$ . The cantilever had a resonance frequency of 419 Hz, Q of 75 and, and  $k = 10^{-3}$  N/m. The gradient magnet was the same one used in the ammonium sulfate experiment with a 400  $\mu\text{m}$  diameter and generating a field of .0647 T and gradient of 350 T/m at 400  $\mu\text{m}$  from the sample. The modest gradient is ideal for obtaining a large signal; high spatial resolution is not required. From these factors we find the force using Curie's law and the field gradient

$$F = \frac{(1.28 \times 10^{15} \text{ borons})(\gamma\hbar)^2(8.0568 + .064671 \text{ T})(350 \text{ T/m})(0.4)\frac{3}{2}(\frac{3}{2} + 1)}{3k_B T} \quad (4.2)$$

where the 0.4 is for 40% of the intensity from the  $-1/2$  to  $1/2$  transition. This yields a force of  $1.39 \times 10^{-13}$  N. The minimum detectable force is then

$$F_{min} = \sqrt{\frac{4(10^{-3} \text{ N/m})k_B T(\frac{1}{4(20 \text{ ms})})}{2\pi(419)(75)}} \quad (4.3)$$

where we used a time constant of 20 ms. This yields a SNR of 8.5 without taking into account any line broadening effects which would further reduce the SNR. While the predicted SNR is small it implies that it appears likely we should be able to see a boron signal at 77 K.

The experiment was performed at 77 K and  $10^{-5}$  torr while waiting 15 s between each CAI and signal averaging 16 times. Assuming that we greater than 10 gauss of  $H_1$  field we set the CAI frequency modulation to 111 kHz to be conservative and stay far from the adiabatic condition. For low temperature NMRFM experiments the NMR coil radiatively heats the cantilever which interferes with artifact levels as well as decreasing force sensitivity. In order to reduce the heating the CAI pulse was reduced to 70 ms from 350 ms in our proton room temperature experiment. In addition we extended the time between pulses to allow the cantilever to cool down between pulses. Also, in the raw data we found that as the gradient magnet approached the sample the cantilever oscillations got larger. This could be attributed to eddy currents in the gradient magnet being formed every time the RF was pulsed. The resulting current would produce magnetic fields that would interact with the oscillator and sample. The resulting oscillations would thus be expected to increase as the magnet got closer since the interaction strength would have increased.

After subtracting out the contribution from the eddy currents the resulting data at 110.9393 MHz and frequency shifted data at 110.7776 MHz is shown in Fig. 4.4. The resonance peak at 110.9393 MHz occurs around  $260 \mu\text{m}$  and has an approximate width of  $60 \mu\text{m}$ . This is approximately  $140 \mu\text{m}$  close than expected, however, this can be attributed to imperfect sample-gradient magnet alignment. The calculated field for our gradient magnet only measures along the  $z$ -axis extending from the center of one face and assumes the cylinder is without defects. The width is reasonable given that the resonance slice

width at that position is approximately  $45 \mu\text{m}$ , thus, there would be considerable overlap in the signal since our sample is about  $30 \mu\text{m}$  thick. Shifting the carrier frequency to  $110.7776 \text{ MHz}$  should have shifted the resonance  $50 \mu\text{m}$  away and indeed we see a shift of approximately  $50 \mu\text{m}$ . The maximum oscillator amplitude, after subtracting out the eddy current contribution, was  $9.5 \text{ nm}$  which corresponds to a force of  $1.2 \times 10^{-13} \text{ N}$ . This is very close to the predicted force, implying that unlike the ammonium sulfate experiment our resonance slice managed to capture nearly all of the sample. The baseline noise was higher than expected, yielding a rough SNR of 4. We do not believe we observed either of the two satellite transition lines since they would have been roughly  $400 \text{ kHz}$  away from the central line which would have corresponded to around  $100$  to  $160 \mu\text{m}$  away which would have been well outside our  $30 \mu\text{m}$  sample.

We next attempted a nutation experiment by varying the length of the pulse before the CAI. Unfortunately we were not able to observe multiple Rabi oscillations; in fact, we could only clearly discern roughly half of a Rabi oscillation whereupon the signal settles into a steady state, see Fig. 4.5. A rough extrapolation from the data yields a  $H_1$  field of  $63 \text{ gauss}$ . This seems plausible since the linewidth in powder samples is approximately  $25 \text{ kHz}$ , which would require at least  $3 \times 18 = 54 \text{ gauss}$  to see a signal.  $63 \text{ gauss}$  represents a much larger increase in  $H_1$  field strength compared to our previous proton experiment and we attribute this to two factors: bringing the sample to within  $150 \mu\text{m}$  of the coil and using a smaller coil.

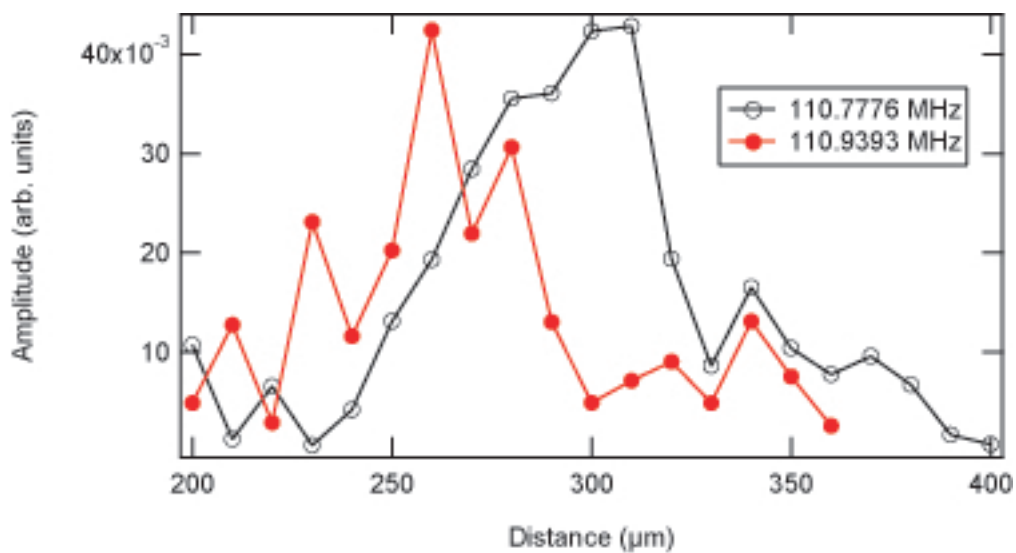


Figure 4.4: 1-D scan of  $\text{MgB}_2$  powder sample with frequency shift to confirm NMR origin of signal

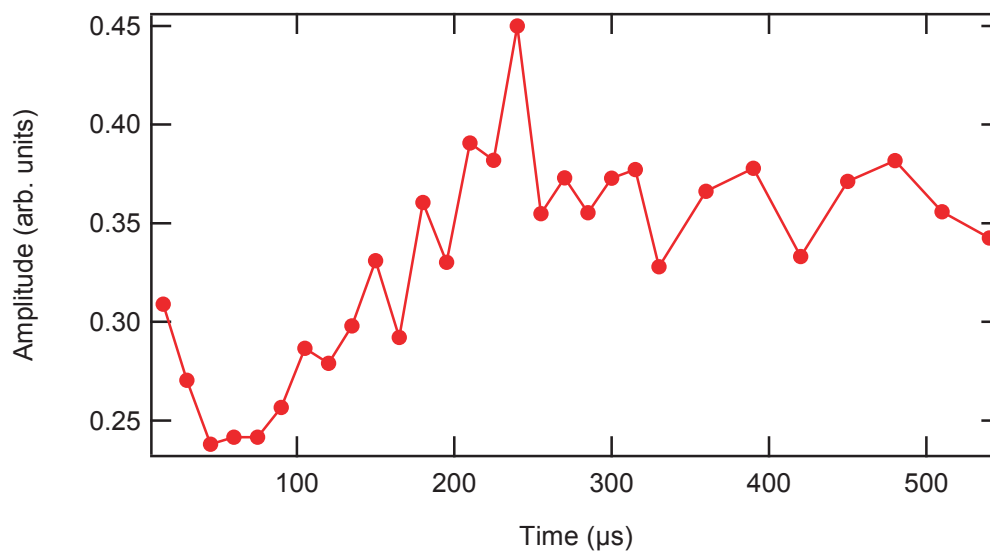


Figure 4.5: Nutation experiment attempt



These results are promising for future NMRFM studies of  $\text{MgB}_2$  since future studies will be performed around the transition temperature of 39 K yielding three times more signal. Greater sensitivity should allow us to better perform spin manipulation experiments such as nutation and spin echoes. In addition, utilizing single crystals should decrease the linewidth and improve the signal strength as well.

## Chapter 5

# Magnetic Measurements of $\text{Mn}_x\text{Sc}_{1-x}\text{N}$ and $\text{Fe}_{0.1}\text{Sc}_{0.9}\text{N}$ , possible dilute magnetic semiconductors

### 5.1 Background

Recently, significant efforts have been made to fabricate dilute magnetic semiconductors (DMS) since they offer a clear path toward the realization of spin-dependent electronics, spintronics. Spintronic devices require a strong coupling between electron charge and spin degrees of freedom. A robust spintronic material will pave the way for new technologies such as spin based transistors as a replacement for MOSFETs. Thus far, efforts to fabricate DMS have concentrated primarily on the (III,V) family of semiconductors with Mn as the dopant. These implanted materials have already shown ferromagnetism at temperatures above 100 K [47] [48]. The Mn ions, in addition to providing ferromagnetism, also serve the role as dopants in the semiconductors and thus alter the conduction of the semiconductor. Ideally, these materials would be fabricated so they exhibit controllable electronic properties and ferromagnetism at room temperature. However, the balance between attaining a high Curie temperature,  $T_C$  and low carrier densities has made this goal difficult. Note here that the  $T_C$  differs from the transition temperature

in superconductors. In ferromagnets, when the temperature rises above the Curie temperature the magnetic ordering vanishes.

Typically DMS fabrication have focused on using GaAs as the semiconductor. However, the zinc blend structure of GaAs possesses low solubility of magnetic impurity atoms causing the occurrence of secondary phases with a crystal structure different from the host. ScN has recently been proposed as an alternative due to its rock salt structure. ScN is an indirect gap semiconductor with an indirect band gap of about 1 eV with a carrier concentration of  $10^{-17}$   $\text{cm}^{-3}$  [49] [50] [51]. MnN also has a rocksalt type structure implying that Mn doped ScN should yield high solubility of Mn atoms, see Fig. 5.1 [52].

Theoretical calculations of the Curie temperature for Mn doped ScN show that it should exceed room temperature for Mn concentrations above 10% [53]. Fig. 5.2 shows the expected  $T_C$ 's for different Mn concentrations using several different calculation methods. We do note that the statistical error is quite large and so there is some doubt as to whether room temperature ferromagnetism is indeed possible. Nevertheless, in conjunction with Arthur Smith's group at Ohio University and Costel Constantin at Seton Hall University we have used molecular beam epitaxy (MBE) to grow  $\text{Mn}_x\text{Sc}_{1-x}\text{N}$  and  $\text{Fe}_{0.1}\text{Sc}_{0.9}\text{N}$  samples and propose to determine whether they exhibit room temperature ferromagnetism and to understand the magnetic interplay between the Mn and the ScN.

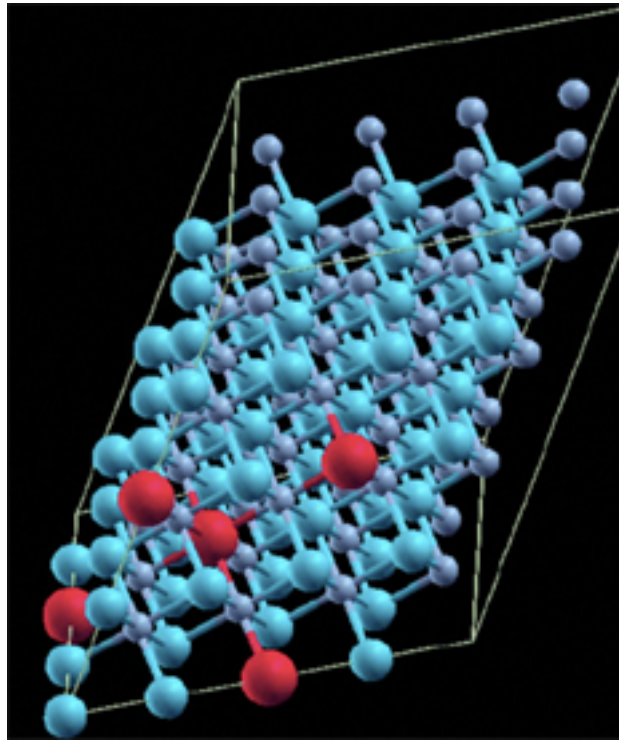


Figure 5.1: Theoretical structure of 8% doped MnScN where Mn are big red balls, Sc medium sized light blue balls, and N small silver balls [7].

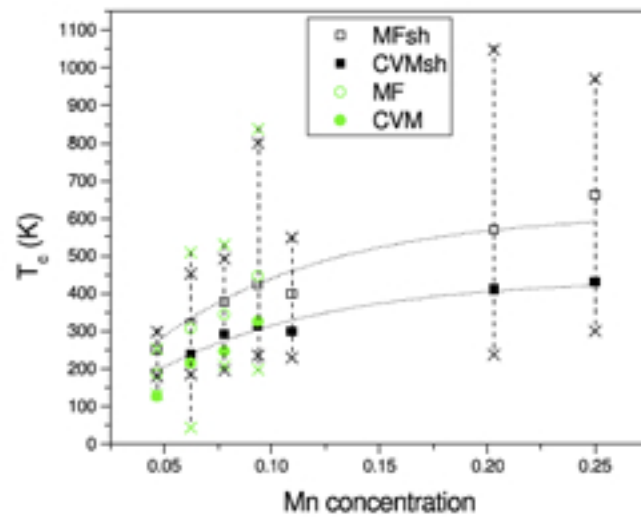


Figure 5.2: Theoretical  $T_C$ 's for different Mn concentration using mean field theory and the cluster variation method. The two green symbols, light colored, use local density approximation and the two black symbols, dark colored, include gap correction. The X symbols indicate the error range. [6]

## 5.2 MBE growth of films

Samples were are using rf-MBE at Ohio University with  $N_2$  as a source gas and utilizing effusion cells for Mn and Sc evaporation. The films are grown on MgO(001) substrates that are heated to  $950^\circ\text{C}$  for 30 minutes with a nitrogen plasma. The buffer layer of ScN is grown at  $800^\circ\text{C}$  with a thickness of approximately 60 nm. Then the temperature is decreased to  $420^\circ$  and the  $Mn_xSc_{1-x}N$  layer is grown with an approximate thickness of 440 nm. Reflection high-energy electron diffraction (RHEED) measurements show a spotty pattern indicating a 3-D growth mode.

## 5.3 SQUID data

We took magnetic moment vs. temperature and field data using a Quantum Design MPMS system with a field range of 0 to 5 T and temperature range up to 365 K. Since the magnetic moments of the films were extremely small the raw data is dominated primarily by the paramagnetic background of the MgO substrate as well as the diamagnetic contribution of the sample holder (i.e. a straw). Background subtractions were performed by assuming a linear in field signal and subtracting it from the raw data.  $M$  vs.  $T$  data was fit to the mean-field scaling function

$$M = A(T_C - T)^{0.33} \quad (5.1)$$

as it describes well the magnetization just below  $T_C$  [54].

Data for the nitrogen poor samples with Mn concentrations of 3% and

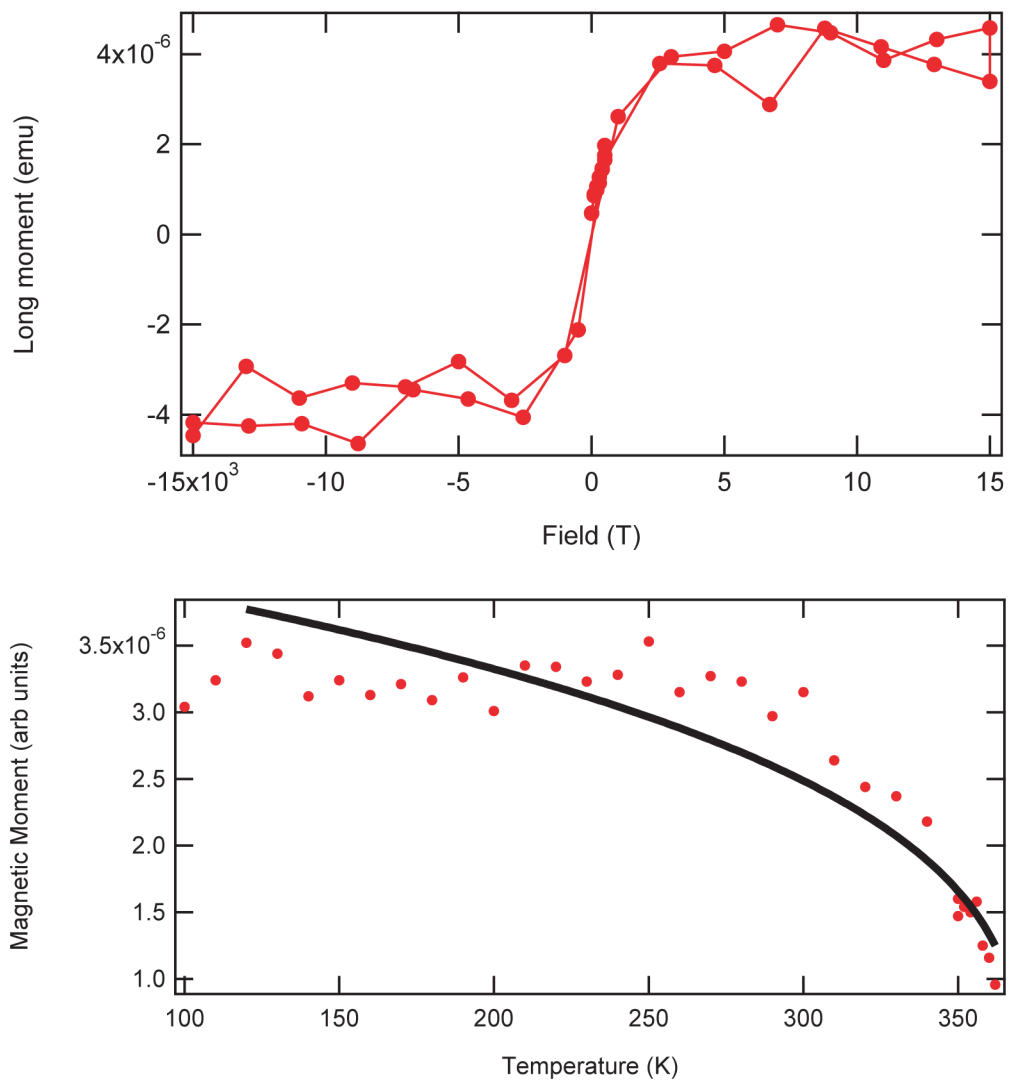


Figure 5.3: Hysteresis and  $M$  v.  $T$  curves for nitrogen poor 3% doped Mn. The hysteresis curve was taken at 350 K.

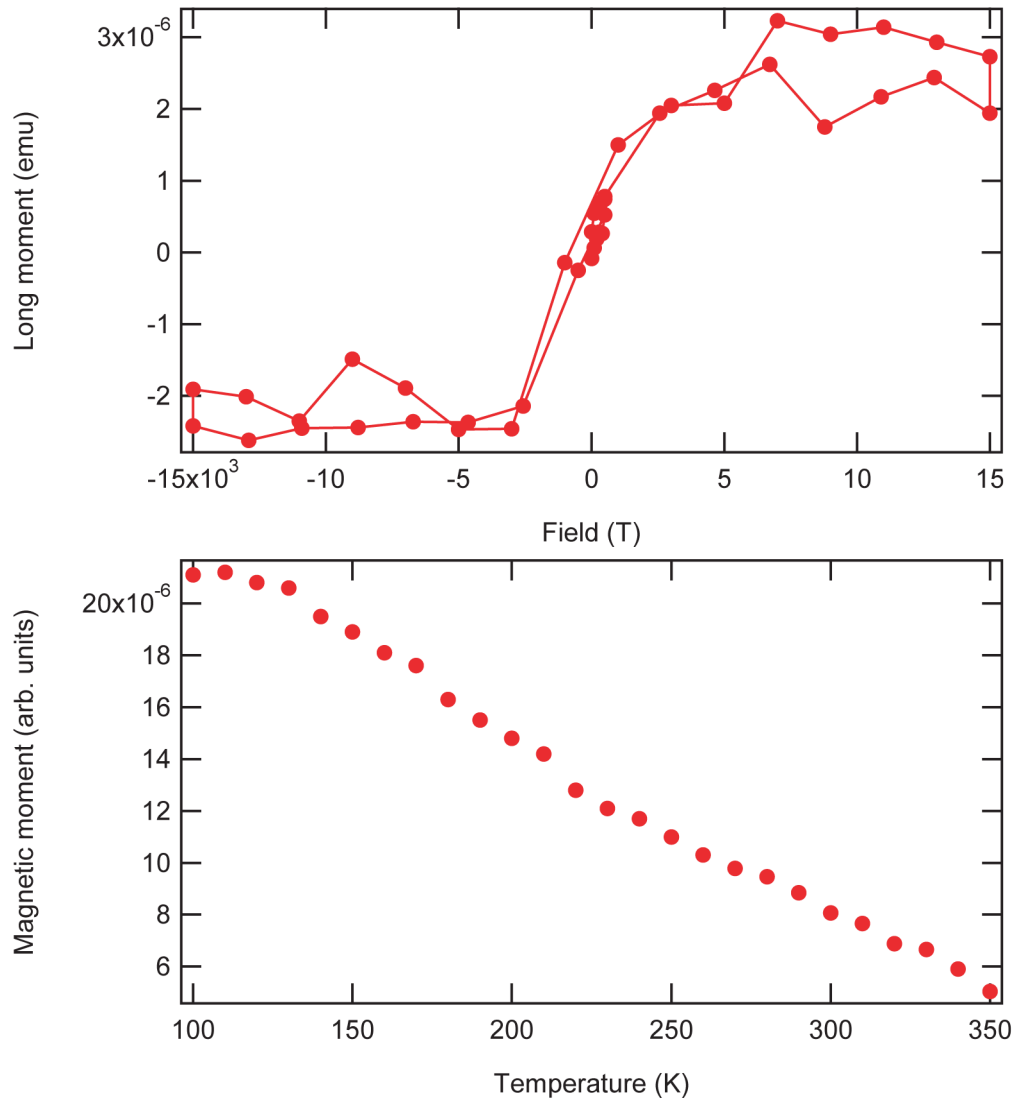


Figure 5.4: Hysteresis and  $M$  v.  $T$  curves for nitrogen poor 15% doped Mn. The hysteresis curve was taken at 340 K.



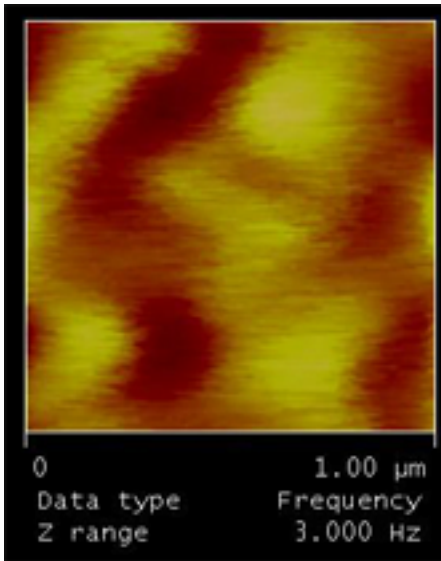


Figure 5.5: MFM image over  $1 \mu\text{m}^2$

15% are shown in Figs. 5.3 and 5.4. Hysteresis curves are evident for both samples indicating the presence of ferromagnetism, however the data are quite noisy since the magnetic signal is relatively small. It is possible that the data indicates paramagnetism or super-paramagnetism, however the overall shape is typical of some ferromagnetism. The  $M$  v.  $T$  data for the 3% sample show a gradual decrease in temperature past 300 K and we are able to fit to Eq. 5.1 yielding an estimated  $T_C$  around 350 K. The fit is not perfect since the magnetic moment seems to be roughly constant below 300 K. Since we are using a mean-field scaling law fit our model may be too ideal and not account for other factors. The  $M$  vs.  $T$  data for the 15% sample steadily decreases starting from 150 K, but it does not conform well to Eq. 5.1 and a fit is not possible and an estimate of  $T_C$  is difficult although magnetism appears to be

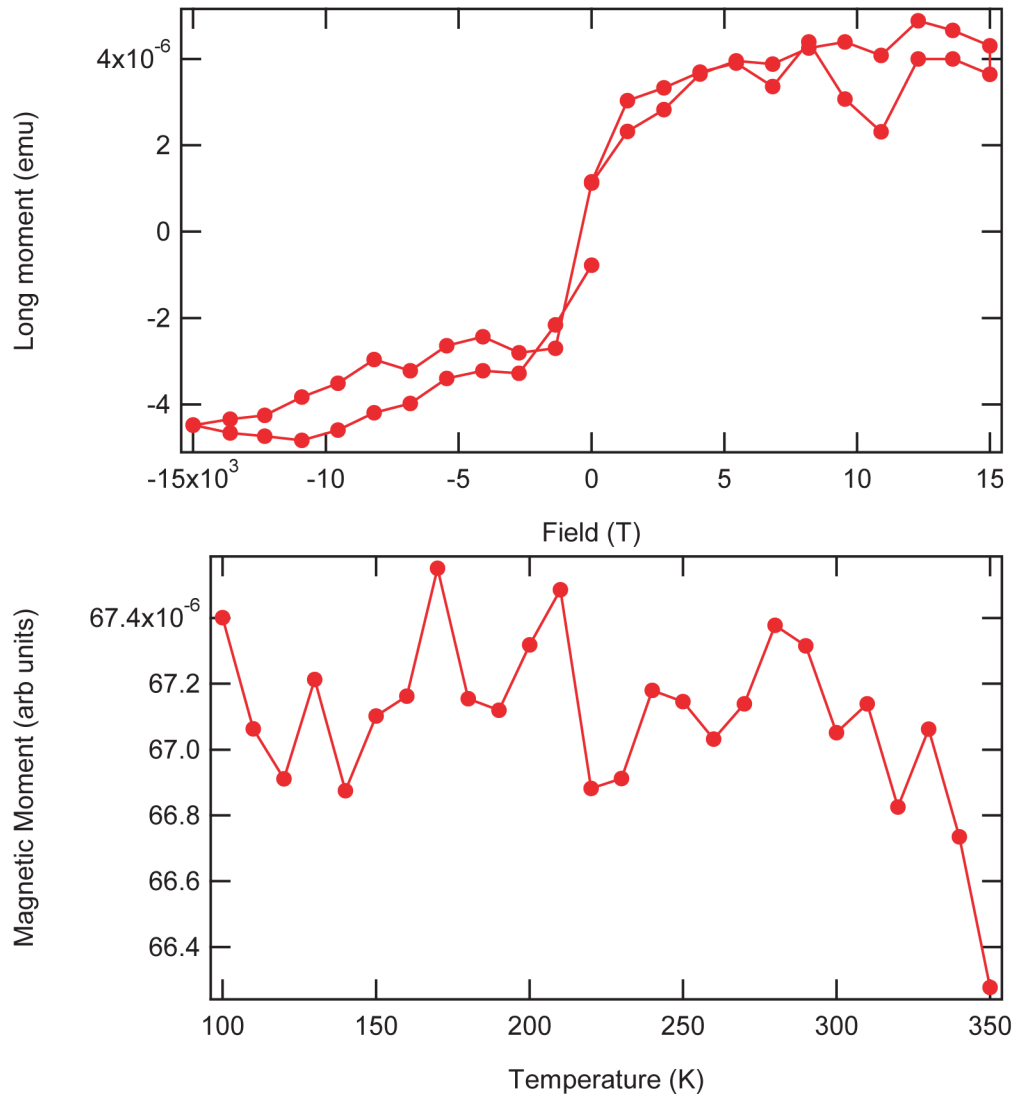


Figure 5.6: Hysteresis and  $M$  v.  $T$  curves for nitrogen rich 3% doped Mn. The hysteresis curve was taken at 350 K.

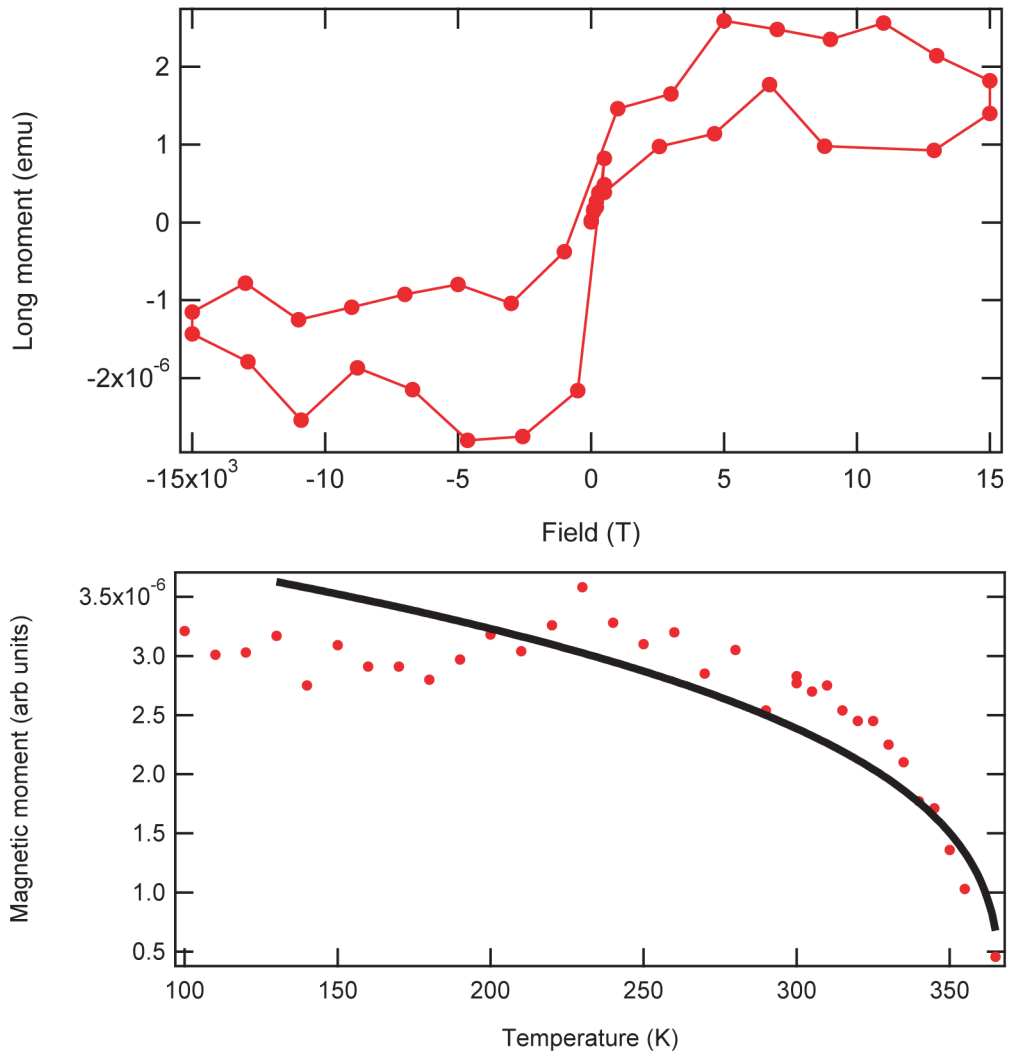


Figure 5.7: Hysteresis and  $M$  v.  $T$  curves for nitrogen poor 5% doped Mn. The hysteresis curve was taken at 340 K.

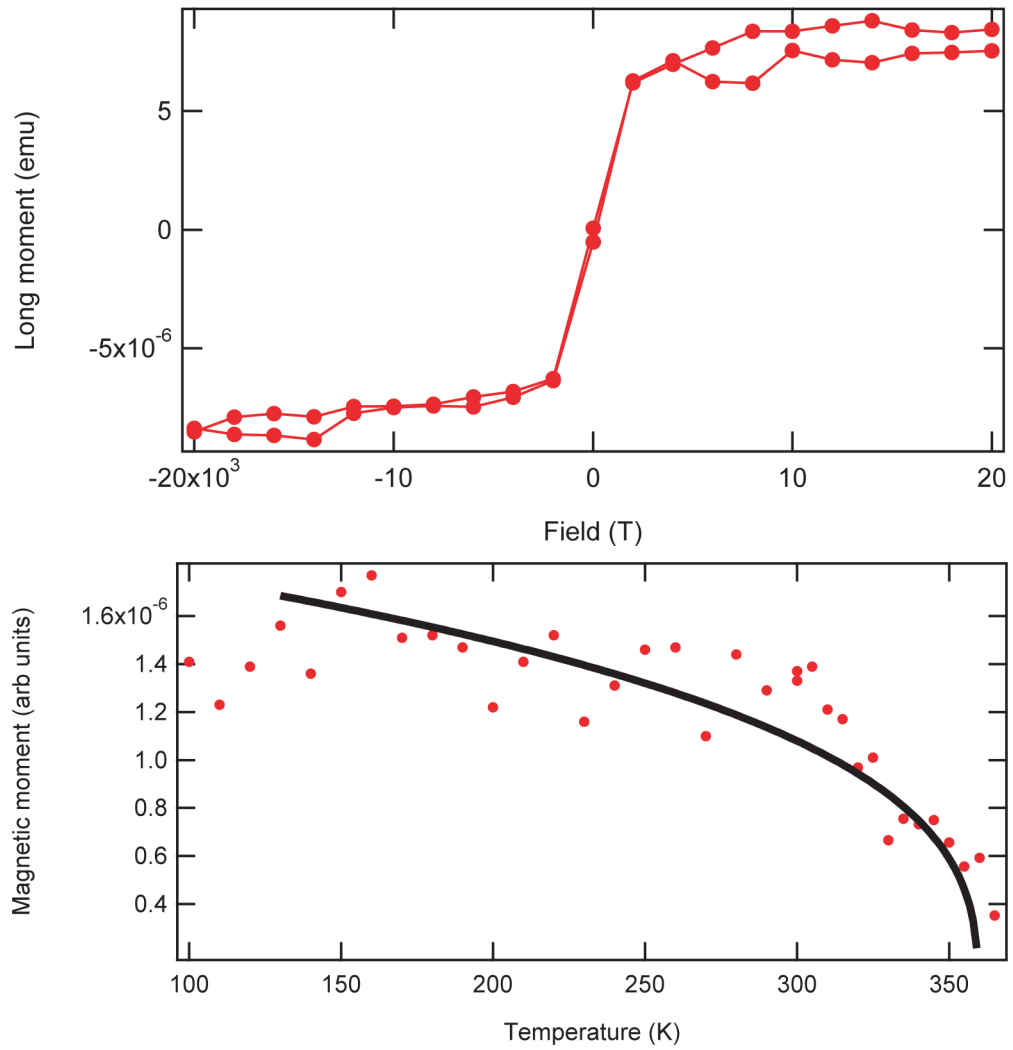


Figure 5.8: Hysteresis and M v. T curves for 1 % Fe-doped samples. The hysteresis curve was taken at 350 K.

present past 350 K. For both nitrogen poor samples it seems there is good evidence for the presence of ferromagnetism past 350 K.

A magnetic force microscopy (MFM) scan, Fig. 5.5, was performed on the nitrogen poor 15% sample at room temperature and magnetic domains appear to be present with widths of several hundred nanometers. The fact that we can see magnetism at room temperature corroborates the SQUID data that shows room temperature magnetism. However, for very thin films we often expect a mono-domain where the magnetism is spread out evenly, and the resulting MFM image to show very little contrast. However, it is possible that the most energetically favorable condition is to clump into domains.

The data for the nitrogen rich samples with Mn concentrations of 3% and 5% are shown in Figs. 5.6 and 5.7. Like the nitrogen poor samples, hysteresis in the  $M$  v.  $H$  data shows the presence of ferromagnetism, although the data is quite noisy. For the 3% samples the  $M$  v.  $T$  data is noisy and a fit to Eq. 5.1 is very poor, although we can infer that magnetism is present past 350 K. Equation 1 fits better for the 5% sample and the  $T_C$  is shown to be above 350 K. Fits to Eq. 5.1 suffer from the same problem that was experienced with the fit to the 3% nitrogen poor samples.

The 10% Fe doped sample in Fig. 8 shows hysteresis at 350 K and a gradual decrease in magnetization as the temperature is increased. However, much like the nitrogen poor samples the magnetization stays essentially constant up to around 300 K before beginning a more dramatic decrease in magnetization. Using Eq. 5.1, we obtain a fairly good fit with an estimated

$T_c$  around 350 K.

In conclusion, it appears that  $\text{Mn}_x\text{Sc}_{1-x}\text{N}$  and  $\text{Fe}_{0.1}\text{Sc}_{0.9}\text{N}$  exhibit magnetism well above room temperature. Further studies need to be carried out to determine if they are indeed dilute magnetic semiconductors. The SQUID data we have taken demonstrates the presence of magnetism, but does not lead us towards an explanation for its presence. TEM and variable temperature magneto-optical Kerr effect (MOKE) and magnetic force microscopy (MFM) studies are needed. Additional studies will also help to elucidate why there apparently seems to be no clear correlation between nitrogen rich, nitrogen poor, and Mn concentrations and  $T_c$ . One possibility is poor sample growth, but there may be other factors that are not apparent through SQUID and room temperature MFM data. Additionally, electrical measurements should be performed to ascertain these materials' value as good semiconductors that may be useful in future spintronic devices.

## Bibliography

- [1] P. Diehl, E. Fluck, H. Gunther, R. Kosfeld, J. Seeling, *Solid-State NMR I: Methods*, Springer (1994).
- [2] A. Abragam, *The Principles of Nuclear Magnetism*, Clarendon Press, Oxford (1961).
- [3] F. Bloch *Phys. Rev.* **70**, 460 (1946).
- [4] H.J. Mamin, R. Budakian, BW Chui, D. Rugar, *Phys. Rev. Lett.* **91**, 207604 (2003).
- [5] D. Rugar, R. Budakian, H.J. Mamin, B.W. Chui, *Nature* **430**, 329 (2004).
- [6] C.P. Slichter, *Principles of Magnetic Resonance*, Springer (1989).
- [7] J.A. Sidles, *Appl. Phys. Lett.* **58**, 2854 (1991).
- [8] G. Binnig, H. Rohrer, Ch. Gerber, and E. Weibel, *Phys. Rev. Lett.* **49**, 57 (1982).
- [9] G. Binnig, C.F. Quate, Ch. Gerber, *Phys. Rev. Lett.* **56**, 930 (1986).
- [10] D. Rugar, C.S. Yannoni, J.A. Sidles, *Nature* **360**, 563 (1992).
- [11] D. Rugar, O. Züger, S. Hoen, C.S. Yannoni, H.-M. Vieth, R.D. Kendrick, *Science* **264**, 1560 (1994).

- [12] N. Nestle, A. Schaff, W.S. Veeman, *Prog. Nucl. Mag. Reson. Spect.*, **38** 1 (2001).
- [13] J.A. Sidles, D. Rugar, *Phys. Rev. Lett.* **70**, 3506 (1993).
- [14] A. Suter, *Prog. Nucl. Magn. Spect.* **45**, 239 (2004).
- [15] C.W. Miller, J.T. Markert, *Phys. Rev. B* **72**, 224402 (2005).
- [16] C. L. Degen, M. Poggio, H. J. Mamin, C. T. Rettner, D. Rugar, *Proc. Nat. Acad. Sci.* **106**, 1313 (2009).
- [17] C.L. Degen, ETH Zurich dissertation (2006).
- [18] Yong Lee, University of Texas at Austin dissertation (2007).
- [19] Curry Taylor, Cornell University dissertation (2008).
- [20] C.L. Degen, U. Meier, Q. Lin, A. Hunkeler, B.H. Meier, *Rev. Sci. Instr.* **77**, 043707 (2006).
- [21] N.E. Jenkins, L.P. DeFlores, J. Allen, T.N. Ng, S.R. Garner, S.Kuehn, J.M. Dawlaty, J.A. Marohn, *J. Vac. Sci. Technol. B* **22(3)**, 909 (2004).
- [22] S. Garner, Cornell University dissertation (2005).
- [23] D. Rugar, H. J. Mamin, P. Guethner, *Appl. Phys. Lett.* **55 (25)**, 2588 (1989)
- [24] Utkur Mirsaidov, University of Texas at Austin dissertation (2005).



- [25] Michelle Chabot, University of Texas at Austin dissertation (2001).
- [26] H.C. Ohanian, J.T. Markert, *Physics for Engineers and Scientists 3rd edition*, Norton (2007).
- [27] O. Klein, G. de Loubens, V. V. Naletov, F. Boust, T. Guillet, H. Hurdequint, A. Leksikov, A. N. Slavin, V. S. Tiberkevich, and N. Vukadinovic, *Phys. Rev. B* **78**, 144410 (2008).
- [28] C.L. Degen, Q. Lin, A. Hunkeler, U. Meier, M. Tomaselli, B.H. Meier, *Phys. Rev. Lett.* **94**, 207601 (2005).
- [29] A.Z. Capri and P.V. Panat, *Introduction to Electrodynamics*, CRC Press (2002).
- [30] Jae-Hyuk Choi, Min-Seok Kim, Yon-Kyu Park, Mahn-Soo Choi, *Appl. Phy. Lett.* **90**, 073117 (2007).
- [31] T.R. Albrecht, P. Gütter, D. Horne, D. Rugar, *J. Appl. Phys.* **69(2)**, 668 (1991).
- [32] G.I. Drandova, University of Texas at Austin dissertation (2001).
- [33] J.L. Cobb, University of Texas at Austin dissertation (1995).
- [34] O. Klein, V.V. Naletov, and H. Alloul, *Euro. Phys. J B* **17**, 57, (2000).
- [35] J. Nagamatsu, N. Nakagawa, T. Muranaka, Y. Zenitani, J. Akimitsu, *Nature* **410**, 63 (2001).

- [36] L.C. Hebel, C.P. Slichter, *Phys. Rev.* **113**, 1504 (1959).
- [37] J. Korringa, *Physica* **16**, 601 (1950).
- [38] R. Walstedt, *The NMR Probe of High- $T_c$  Materials*, Springer (2008).
- [39] M. Tinkham, *Introduction to Superconductivity*, Dover (1996).
- [40] H. Kotegawa, K. Ishida, Y. Kitaoka, T. Muranaka, J. Akimitsu, *Phys. Rev. Lett* **87**, 127001 (2001).
- [41] S.H. Baek, B.J. Suh, E. Pavarini, F. Borsa, R.G. Barnes, S.L. Bud'ko, P.C. Canfield, *Phys. Rev. B* **66**, 104510 (2002).
- [42] J.K. Jung, S.H. Baek, F. Borsa, S.L. Bud'ko, G. Lapertot, P.C. Canfield *Phys. Rev. B* **64**, 012514 (2001).
- [43] S. Strassle, J. Roos, M. Mali, H. Keller, J. Karpinski, *Physica C* **466**, 168 (2007).
- [44] M. Tillman, G. Lapertot, R. Prozorov, C. Martin, S.L. Bud'ko, P.C. Canfield, March Meeting Abstract A11.00007 (2008).
- [45] C.P. Slichter, *Principles of Magnetic Resonance*, p. 499, Springer (1990).
- [46] A. Abragam, *The Principles of Nuclear Magnetism*, Clarendon Press, Oxford (1961).
- [47] H. Ohno, *Science* **281**, 951 (1998).

- [48] K.Y. Wang et al., *AIP Conf. Proc.* **772**, 333 (2005).
- [49] T.D. Moustakas, R.J. Molnar, J.P. Dismukes, *Electrochem. Soc. Proc.* **96-11**, 197 (1996).
- [50] H. Al-Brithen, A.R. Smith, *Appl Phys. Lett.* **77**, 2485 (2000).
- [51] A.R. Smith, H.A.H. Al-Brithen, D. C. Ingram, D. Gall, *J. Appl. Phys.* **90**, 1809 (2001).
- [52] A. Leineweber, R. Niewa, H. Jacobs, W. Kocklemann, *J. Mater. Chem.* **10**, 2827 (2000).
- [53] A. Herwadkar, W.R.L. Lambrecht, M. van Schilfgaarde, *Phys. Rev. B* **77**, 134433 (2008).
- [54] N.W. Ashcroft, N.D. Mermin, *Solid State Physics*, Brooks-Cole, p. 699 (1976).

## Appendices

## Appendix

When we order the stack piezos we order the room temperature versions (NEC Tokin) in order to save money off the low temp ones (Piezomechanik) which are considerably more expensive and have thick wires that can get ripped off easily. The room temperature piezos possess a coating that supposedly protects it, but is inconvenient for low temperature use since it will crack. In order to remove the coating we soak the piezos in acetone for 12-24 hours. This effectively softens up the coating which can now be easily removed with a razor. If you happen to nick off one of the wires while removing the coating, clamp the wire back onto the piezo with an alligator clip and then use H21D epoxy to secure the exposed end of the wire to the contact point of the piezo.

## Vita

Han-Jong Chia was born in San Jose, CA on September 24, 1982. He attended Grinnell College and received B.A.s in Physics and Economics in 2004. Since he found physics more exciting than economics he applied to and was accepted to the physics department at the University of Texas at Austin in 2004. Since then he has worked in the lab of John T. Markert focusing primarily on NMRFM. After graduation he will work with Robert McMichael at NIST, Gaithersburg on FMRFM.

Permanent address: 4749 Williams Rd.  
San Jose, CA 95129

This dissertation was typeset with L<sup>A</sup>T<sub>E</sub>X<sup>†</sup> by the author.

---

<sup>†</sup>L<sup>A</sup>T<sub>E</sub>X is a document preparation system developed by Leslie Lamport as a special version of Donald Knuth's T<sub>E</sub>X Program.